

Study of hydrated asteroids via their polarimetric properties at low phase angles

Jooyeon Geem^{1,2}, Masateru Ishiguro^{1,2}, Hiroyuki Naito³, Sunao Hasegawa⁴, Jun Takahashi⁵, Yoonsoo P. Bach⁶, Sunho Jin^{1,2}, Seiko Takagi⁷, Tatsuharu Ono⁷, Daisuke Kuroda⁸, Tomohiko Sekiguchi⁹, Kiyoshi Kuramoto⁷, Tomoki Nakamura¹⁰, and Makoto Watanabe¹¹

¹ Department of Physics and Astronomy, Seoul National University, 1 Gwanak-ro, Gwanak-gu, Seoul 08826, Republic of Korea

² SNU Astronomy Research Center, Seoul National University, 1 Gwanak-ro, Gwanak-gu, Seoul 08826, Republic of Korea

³ Nayoro Observatory, 157-1 Nisshin, Nayoro, Hokkaido 096-0066, Japan

⁴ Institute of Space and Astronautical Science (ISAS), Japan Aerospace Exploration Agency (JAXA), Sagami-hara, Kanagawa 252-5210, Japan

⁵ Center for Astronomy, University of Hyogo, 407-2 Nishigaichi, Sayo, Hyogo 679-5313, Japan

⁶ Korea Astronomy and Space Science Institute (KASI), 776 Daedeok-daero, Yuseong-gu, Daejeon 34055, Republic of Korea

⁷ Department of CosmoSciences, Graduate School of Science, Hokkaido University, Kita-ku, Sapporo 060-0810, Japan

⁸ Bisei Spaceguard Center, Japan Spaceguard Association, 1716-3 Okura, Bisei-cho, Ibara, Okayama 714-1411, Japan

⁹ Asahikawa Campus, Hokkaido University of Education, Hokumon, Asahikawa, Hokkaido 070-8621, Japan

¹⁰ Department of Earth and Planetary Material Sciences, Faculty of Science, Tohoku University, Aoba, Sendai, Miyagi 980-8578, Japan

¹¹ Department of Physics, Okayama University of Science, 1-1 Ridai-cho, Kita-ku, Okayama, Okayama 700-0005, Japan

Received 15 Apr 2024 / Accepted 30 May 2024 / Last modified 26 May 2024

ABSTRACT

Context. Ch-type asteroids are distinctive among other dark asteroids in that they exhibit deep negative polarization branches (NPBs). Nevertheless, the physical and compositional properties that cause their polarimetric distinctiveness are less investigated.

Aims. We aim to investigate the polarimetric uniqueness of Ch-type asteroids by making databases of various observational quantities (i.e., spectroscopic and photometric properties as well as polarimetric ones) of dark asteroids.

Methods. We conducted an intensive polarimetric survey of 52 dark asteroids (including 31 Ch-type asteroids) in the R_C -band to increase the size of polarimetric samples. The observed data are compiled with previous polarimetric, spectroscopic, and photometric archival data to find their correlations.

Results. We find remarkable correlations between these observed quantities, particularly the depth of NPBs and their spectroscopic features associated with the hydrated minerals. The amplitude of the opposition effect in photometric properties also shows correlations with polarimetric and spectral properties. However, these observed quantities do not show noticeable correlations with the geometric albedo, thermal inertia, and diameter of asteroids.

Conclusions. Based on the observational evidence, we arrive at our conclusion that the submicrometer-sized structures (fibrous or flaky puff pastry-like structures in phyllosilicates) in the regolith particles could contribute to the distinctive NPBs of hydrated asteroids.

Key words. Polarization – Techniques: polarimetric – Minor planets, asteroids

1. Introduction

It is important to understand C-complex asteroids because they are regarded as primitive asteroids due to their spectra analogous to those of volatile-rich meteorites (i.e., carbonaceous chondrites, Gaffey & McCord 1979). These asteroids are the most massive group in the main belt, accounting for more than half of the total mass of the belt (DeMeo & Carry 2013). Previous ground-based observations have revealed evidence of the hydrated minerals (mainly phyllosilicates) as a result of aqueous alteration activity (Gaffey & McCord 1979; Lebofsky et al. 1990; Jones et al. 1990; Rivkin et al. 2002; DeMeo et al. 2009; Fornasier et al. 2014; Takir et al. 2015) from C-complex asteroids. The Japanese infrared satellite AKARI further confirmed that most of the observed C-complex asteroids in the main belt (17 out of 22) show the spectral feature associated with the hydrated mineral (Usui et al. 2019). Moreover, in the early 2020s,

JAXA's Hayabusa2 and NASA's OSIRIS-REx sample return missions visited Near-Earth asteroids (NEAs) (162173) Ryugu and (101955) Bennu, respectively, and found the widespread hydrated minerals on NEAs via the in situ observation and laboratory analysis (Hamilton et al. 2019; Noguchi et al. 2023). Consequently, studies via ground-based observation, space telescopes, space missions, and laboratories so far imply that a significant fraction of the C-complex across the Solar System could be asteroids with hydrated minerals (i.e., hydrated asteroids).

Hydrated asteroids have been extensively studied via spectroscopy. The spectral features indicating the hydrated minerals include absorption features in the UV region (also known as UV drop-off), around $0.7\ \mu\text{m}$ and $2.7\ \mu\text{m}$ (Rivkin et al. 2002). Particularly, the asteroids with the absorption band of $\sim 0.7\ \mu\text{m}$ are defined as Ch- or Cgh-type asteroids in the SMASSII and Bus-DeMeo classifications (Bus & Binzel 2002; DeMeo et al. 2009).

Cgh-type asteroids have a more pronounced UV drop-off than those of Ch-types. In this paper, for convenience, we refer to both Ch- and Cgh-type asteroids as Ch-type asteroids. Ch-type asteroids are generally regarded as strongly hydrated asteroids due to the prominent UV drop-off and absorption features near $2.7\ \mu\text{m}$ observed in the majority of Ch-type asteroids (Tholen 1984; Vilas 1994; Fornasier et al. 2014; Takir et al. 2015). Additionally, Ch-type asteroids are believed to be parent bodies of CM-type meteorites (i.e., hydrated meteorites) due to their analogous spectra from UV to the near-infrared range (Gaffey & McCord 1979).

On the other hand, it is known that Ch-type asteroids exhibit unique polarimetric characteristics. In general, the polarimetric properties have been characterized by the linear polarization degree with respect to the scattering plane of asteroids (P_r) as a function of the phase angle (α , the angle between the sun, target, and observer) (Dollfus & Geake 1977). At low phase angles ($\alpha \lesssim 20^\circ$), most asteroids exhibit negative P_r values (i.e., light polarized in a parallel direction to the scattering plane). In this paper, we call this region a negative polarization branch (NPB). In NPB, P_r decreases as α increases until reaching the minimum (P_{\min}) at the minimum phase angle (α_{\min}) and gradually ascends and shows a positive P_r value (i.e., light polarized in a perpendicular direction to the scattering plane) at $\alpha > \alpha_0$. α_0 is the so-called inversion angle where the P_r becomes zero, typically occurring around $\alpha \sim 20^\circ$ (Cellino et al. 2015; Belskaya et al. 2017). The slope of the $P_r(\alpha)$ profile at α_0 is called the polarimetric slope h . Gil-Hutton & Cañada-Assandri (2012) compared the NPBs of 39 C-complex asteroids and found that different subsets within the C-complex (i.e., Cb-, Ch-, and C-types) have different NPB profiles. Later, Belskaya et al. (2017) conducted a comprehensive NPB survey of different types of asteroids and found that Ch-type asteroids exhibit distinctively deep NPBs compared to other asteroids with similar albedo (e.g., P-, B-, F-type, and C-complex asteroids). More recently, Kwon et al. (2023) also pointed out that the hydrated C-complex asteroids have particularly deep NPBs. The distinctive polarimetric properties observed on hydrated asteroids may be related to their unique surface properties. The polarimetric properties of asteroids are the result of surface scattering phenomena, providing insight into both their surface composition and surficial physical properties such as grain size or porosity (Ito et al. 2018; Kuroda et al. 2021; Hadamcik et al. 2023; Bach et al. 2024a, and references therein). For example, it is known that the geometric albedo at the V -band (p_V , primarily determined by surface composition) has a good correlation with polarimetric parameters (h and P_{\min} , Zellner et al. 1977; Dollfus 1998; Lupishko & Mohamed 1996; Cellino et al. 2015). Particularly, h shows a tight correlation with p_V , making h widely used in deriving the albedo of the targets (Widorn 1967; Cellino et al. 2015; Lupishko 2018). Additionally, Belskaya et al. (2017) found that the same spectral taxonomy types of asteroids have a comparable P_{\min} and α_0 , suggesting that polarimetry can be utilized as a method to distinguish asteroid taxonomic types. Ishiguro et al. (2022) found that the anhydrous and hydrated meteorites are distributed in different locations in the P_{\min} - h diagram, suggesting that polarimetry can distinguish the anhydrous and hydrated properties. Meanwhile, polarimetry can also provide insights into surface physical properties. For example, Geake & Dollfus (1986) found that the lunar samples in different forms have different P_{\min} and α_0 values. Geake & Geake (1990) also noted that if the grain size of samples approaches or decreases below the wavelength scale of light, the NPB gets much deeper. These empirical relationships between polarimetric parameters and surface characteristics pro-

vide information on the asteroidal surface. Thus, the unique polarimetric properties of hydrated asteroids may reflect their distinctive surface in terms of composition, physical properties, or both.

However, only a few polarimetric studies targeted the hydrated asteroids (Chapman et al. 1975; Gil-Hutton & Cañada-Assandri 2012; Belskaya et al. 2017; Kwon et al. 2023). In particular, the physical and compositional properties that cause the polarimetric distinctiveness of hydrated asteroids have yet to be investigated well in the published literature. In addition, there are only a limited number of Ch-type polarimetric samples whose NPB parameters have been obtained. Gil-Hutton & Cañada-Assandri (2012) only provided the mean polarimetric parameters for Ch-type asteroids. Belskaya et al. (2017) derived the NPBs parameters individually but only nine Ch-type asteroids are analyzed, while Kwon et al. (2023) focuses on only large C-complex asteroids (≥ 100 km in diameter). In this work, we aim to deepen our understanding of the possible surface properties of the hydrated asteroids that cause their pronounced NPBs by increasing the observation samples. We conducted polarimetric observations focusing on C-complex asteroids, including Ch-type asteroids, to increase the sample size and to cover a wide range of conditions within the C-complex asteroids, such as diameters. We then merged the available polarimetric, spectral, and photometric data with our observations and archived them to make a comprehensive database of various observation quantities to see the correlation between them. In the database, we included the data of dark asteroids ($p_V \lesssim 0.12$) consisting of the asteroids classified as G-, B-, F-, P-, or D-types and C-complex in Tholen, SMASSII, or Bus-DeMeo classifications (Tholen 1984; Bus & Binzel 2002; DeMeo et al. 2009). These asteroid types are thought to be primitive due to their spectra similar to carbonaceous chondrites (Gaffey & McCord 1979; Hiroi et al. 2001). In Sect. 2, we describe our observation, data analysis, and how we process the observational quantities from the archives. In Sect. 3, we report our findings, and in Sect. 4 interpret our findings.

2. Method

2.1. Polarimetric observations and data reduction

We conducted polarimetric observations for 50 nights from 2020 March 23 to 2023 November 02. During this period, we observed 52 dark asteroids (asteroids with the geometric albedo $p_V \lesssim 0.12$), including 31 Ch-type asteroids (DeMeo et al. 2009; Hasegawa et al. 2024).

The observation circumstance is summarized in Tables C1. Because polarimetry data for Ch-type asteroids were insufficient before our survey, we intended to increase the sample number of P_{\min} , h , and α_0 of this asteroid type. Thus, we coordinated our polarimetry to observe asteroids (a) whose polarimetric data has not been reported, (b) observable at the positive branch, or (c) observable at the $\alpha \sim 10^\circ$. Examples of the observational results based on these conditions are shown in Fig. 1a–c. Condition (b) enables us to derive h and α_0 , while condition (c) allows us to derive P_{\min} because this type of asteroid usually indicates the polarization minima around $\alpha \sim 10^\circ$ (Belskaya et al. 2017).

We conducted the observations with two telescopes: the 1.6-m Pirka Telescope in the Nayoro Observatory (NO) of the Faculty of Science, Hokkaido University (code number Q33) and the 2.0-m Nayuta telescope in the Nishi-Harima Astronomical Observatory (NHAO), in Japan. The polarimetric instruments are installed on the Cassegrain focus of each telescope.

We used a Multi-Spectral Imager (MSI; Watanabe et al. 2012) in NO. This instrument equips a Wollaston beam splitter (WBS), a rotatable half-wave plate (HWP), and a polarization mask to obtain polarimetric images. The WBS has the advantage of reducing the influence of time-dependent atmospheric extinction. The polarization mask divides the field of view (FOV) into two areas to prevent ordinary and extraordinary signal mixing. The FOV and pixel scale are $3.3' \times 0.7'$ and $0.39'' \text{ pixel}^{-1}$, respectively. We used mainly the R_C -band filter for the observations.

At NHAO, we used a Wide Field Grism Spectrograph 2 (WFGS2; Uehara et al. 2004; Kawakami et al. 2022) in the polarization mode by inserting a polarization slit, HWP, and WBS. Each image consists of two panels, ordinary and extraordinary signals. Each panel has a FOV of $6.8' \times 3.0'$ with a pixel scale of $0.198'' \text{ pixel}^{-1}$.

For all observations in this study at NO and NHAO, we took polarization images at four different HWP angles (θ_{HWP}) in the sequence of $\theta_{\text{HWP}} = 0^\circ, 45^\circ, 22.5^\circ$ and 67.5° to derive the Stokes parameters, Q/I and U/I . All observations were performed in the asteroid tracking mode.

We analyzed these data, following the procedure written in Ishiguro et al. (2022) and Geem et al. (2022a). However, it should be noted that we modified a part of the data analysis pipeline for the MSI data taken after 2021 March. In this period, we noticed that the WBS of MSI was not fixed firmly after a replacement of the WBS on 2021 March 2. As a result, the positions of the ordinary ray (o-ray) and the extraordinary ray (e-ray) changed on the detector due to a rotation of the WBS in the filter wheel. This rotation allowed us to add additional correction steps to the analysis procedure. This WBS rotation happened frequently in 2023 June–November. Through observations of standard stars, we established a technique to correct instrumental polarization and the position angle offset of MSI properly by giving the rotation angle of the WBS (which can be derived from each observed image by measuring the relative positions of the o-ray and e-ray components) as a parameter. The detailed analysis and the updated data reduction procedure are given in Appendix A. We also opened our data reduction script files on GitHub¹.

2.2. Derivation of polarimetric parameters

We derived the nightly averaged P_r and summarized the results in Tables D1. Our observations were mainly conducted in the R_C -band. Because most of the previous observations by other groups were conducted in the V -band, we examined the wavelength dependency in P_r . For 26 dark asteroids with a small uncertainty ($\sigma P_r < 0.1\%$), we found negligible P_r differences ($1\sigma = 0.108\%$) in these V - and R_C -bands (see Appendix B). For this reason, we compiled our R_C -band P_r data with other's V -band P_r data despite the wavelength difference. Fig. 1 shows examples of the polarization phase curves (PPCs) for three asteroids.

Fig. 1a is the example where we took all of the data points that cover around the α_{min} and α_0 . Fig. 1b and c are examples where we coordinated our observation to cover the α_0 or α_{min} .

We characterized the observed PPCs around the NPBs by deriving four key parameters: P_{min} , α_{min} , h and α_0 . We fitted the PPCs of each asteroid using the modified linear-exponential function (Bach et al. 2024b). The modified function is derived from the original linear-exponential function (Muinonen et al.

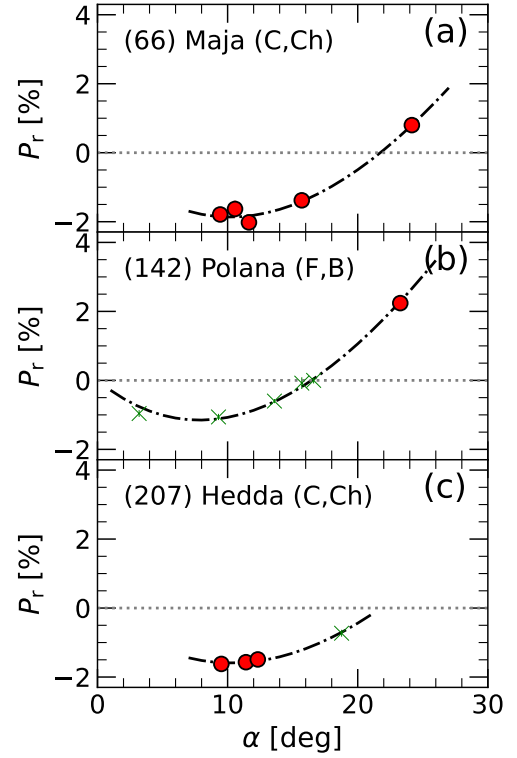


Fig. 1. Selected PPCs for three asteroids: (a) (66) Maja, (b) (142) Polana, and (c) (207) Hedda. These spectral types are given in parentheses based on the Tholen and Bus-DeMeo classifications. The red-filled circles are R_C -band P_r data acquired in this study, while the green crosses are V -band P_r data from previous research. These data points were fitted using the modified linear-exponential function (see Eq. (1) in Sect. 2.2) despite the discrepancy in the filters. The fitting profiles are shown by the dashed lines.

2009), with the free parameters of the original function re-parameterized to reflect the polarimetric parameters of interest. The modified function is given by

$$P_r(\alpha) = h \frac{(1 - e^{-\alpha_0/k})\alpha - (1 - e^{-\alpha/k})\alpha_0}{1 - (1 + \alpha_0/k)e^{-\alpha_0/k}}, \quad (1)$$

where h , α_0 and k are the free parameters for fittings. From Eq. (1), we can obtain α_{min} given by

$$\alpha_{\text{min}} = -k \ln \left\{ \frac{k}{\alpha_0} (1 - e^{-\alpha_0/k}) \right\}, \quad (2)$$

and $P_{\text{min}} = P_r(\alpha_{\text{min}})$. Eq. (2) originates from Bach et al. (2024b). We fitted the data both from our observations and previous research (Gil-Hutton, R. & García-Migani, E. 2017; Lupishko 2019; Bendjoya et al. 2022; Kwon et al. 2023) by using the Markov chain Monte Carlo (MCMC) which is the well-established method for solving the global optimization problem. We employed MCMC implemented in PyMC (Oriol et al. 2023) with 5 000 samples per chain with four chains and the boundary conditions of $0.01\% \text{ deg}^{-1} < h < 0.5\% \text{ deg}^{-1}$, $10^\circ < \alpha_0 < 30^\circ$, and $0^\circ < k < 500^\circ$ and with the initial condition of $h = 0.2\% \text{ deg}^{-1}$, $\alpha_0 = 20^\circ$ and $k = 100^\circ$. To fit the PPCs, we limited the phase angle range $\alpha < 35^\circ$ for the observed data. The best-fit phase curves and their $1-\sigma$ uncertainties are derived based on the 50th, 16th, and 84th percentiles of the samples in the marginalized distribution. Because the linear-exponential function model

¹ https://github.com/Geemjy/Geem_AA_2024

in Eq. (1) is empirical, the parameters that are derived by the extrapolation are likely less reliable. For this reason, only the values of P_{\min} , h , α_0 , and α_{\min} obtained by interpolation were adopted as results in this study and used in the following scientific discussion (see the fitted PPCs in Fig. 1 as examples). The polarimetric parameters that are newly reported or updated by this study are summarized in Table 1.

Some asteroids had fewer than three P_r data points, making it mathematically impossible to fit the data using Eq. (1). As we mentioned above, it is known that the majority of asteroids have α_{\min} around 10° (Belskaya et al. 2017). Therefore, we derived the P_r value of ten asteroids obtained around a phase angle of 10° (i.e., $8^\circ < \alpha < 12^\circ$) as a proxy of the P_{\min} . These asteroids are (209) Dido, (442) Eichsfeldia, (618) Elfriede, (771) Libera, (821) Fanny, (1015) Christa, (1542) Schalen, (1754) Cunningham, (1795) Woltjer, and (2560) Madeline. The P_{\min} values obtained in this way (P_{\min}^*) are marked in Table 1. However, the uncertainties of P_{\min}^* may not be derived correctly, thus we do not use P_{\min}^* for our analyses and discussion, such as deriving correlation coefficients. Additionally, among our target asteroids, (1867) Deiphobus has only a single P_r data point at an α of 6.82° . Due to the lack of data, its polarimetric parameters are not derived for (1867) Deiphobus.

In addition, we calculated the polarimetric parameters for asteroids whose polarimetric data are available in the literature (Gil-Hutton, R. & García-Migani, E. 2017; Lupishko 2019; Bendjoya et al. 2022; Kwon et al. 2023) by using the same fitting algorithm. In this way, we unified the method to derive P_{\min} , h , α_0 , and α_{\min} of all asteroids and eliminate the possible bias resulting from the different fitting processes (e.g., adopting the different fitting functions, methods to derive the uncertainty, and the fitting algorithm). The derived polarimetric parameters of all asteroids analyzed in this study are available via <http://cdsarc.u-strasbg.fr/viz-bin/cat/J/A+A/XXX/XXX>.

2.3. Preparation of spectroscopic data

To understand the polarimetric properties we derived above (Sect. 2.2), we compared them with their spectral features. We made use of the archival spectral data given in Tholen (1984); Zellner et al. (1985); Bus & Binzel (2002); DeMeo et al. (2009); Takir & Emery (2012); Fornasier et al. (2014); Takir et al. (2015), and Usui et al. (2019). We focused on three spectral features indicating the hydrated asteroids: the *UV* drop-off feature appearing in the ultraviolet to visible range, the broad absorption feature around $0.7 \mu\text{m}$, and the absorption feature around $2.7 \mu\text{m}$ (Rivkin et al. 2000, 2002; Fornasier et al. 2014; Usui et al. 2019; Tatsumi et al. 2023).

To characterize the *UV* drop-off, we utilized the Eight Color Asteroid Survey (ECAS, Zellner et al. 1985; Tholen 1984; Zellner et al. 2020) data. The ECAS spectrophotometric data cover a wide wavelength range from $0.31 \mu\text{m}$ to $1.04 \mu\text{m}$ and adequately characterize the *UV* drop-off. As a proxy of the *UV* drop-off, we calculated the ratio of reflectance at $0.32 \mu\text{m}$ and $0.55 \mu\text{m}$. Because most carbonaceous asteroids have a *UV* drop-off, the ratio (\hat{R}_{UV}) is usually ≤ 1 .

To examine the $0.7 \mu\text{m}$ absorption feature, we derived the reflectance after the spectral slope correction. We used the spectral data from three sources: ECAS, Small Main-Belt Asteroid Spectroscopic Survey (SMASS, Bus & Binzel 2002; Rayner et al. 2003), and Fornasier et al. (2014). For ECAS data, we corrected the spectral slope from $0.545 \mu\text{m}$ (v-band) to $0.860 \mu\text{m}$ (x-band) by fitting them using a linear function, divided the original spectral data by the fitted function, normalized them at $0.545 \mu\text{m}$,

and derived the reflectance at $0.705 \mu\text{m}$ (w-band). This process is given by

$$\hat{R}_\lambda = \frac{R_\lambda}{S_\lambda}, \quad (3)$$

where R_λ and \hat{R}_λ are the reflectance at the wavelength of λ in μm and the residual reflectance created as a result of the R_λ divided by the S_λ , respectively. Here, S_λ is the linear function given by

$$S_\lambda = \frac{(R_{0.86} - R_{0.55})}{(0.86 \mu\text{m} - 0.55 \mu\text{m})}(\lambda - 0.55 \mu\text{m}) + R_{0.55}. \quad (4)$$

We chose $\hat{R}_{0.7}$ to characterize the $0.7 \mu\text{m}$ band in the following discussion. A similar method was applied to the SMASS data. We obtained the averaged reflectances at $0.55 \mu\text{m}$, $0.70 \mu\text{m}$, and $0.86 \mu\text{m}$ ($R_{0.55}$, $R_{0.7}$, and $R_{0.86}$) by calculating the median values and standard deviations of the SMASS spectra in the range of 0.55 ± 0.025 , 0.70 ± 0.025 and $0.86 \pm 0.025 \mu\text{m}$, respectively. Then, we obtained $\hat{R}_{0.7}$ by using Eqs. (3), (4). Fornasier et al. (2014) provide the band depth (%), $\text{BD}_{\text{for}14}$ at $0.7 \mu\text{m}$. To match the definition in this study, we calculated $\hat{R}_{0.7} = (100 - \text{BD}_{\text{for}14})/100$. If $\hat{R}_{0.7}$ is available from multiple references, we use their average values.

While deriving $\hat{R}_{0.7}$ from three different sources (i.e., ECAS, SMASS, and Fornasier et al. 2014), we noticed significant inconsistencies among the $\hat{R}_{0.7}$ values from the different references. For example, (50) Virginia has the $\hat{R}_{0.7}$ values of 0.97 ± 0.01 in SMASS and 1.04 ± 0.03 in ECAS (Tholen 1984; DeMeo et al. 2009). That means, depending on the references, (50) Virginia has spectra shape of either convex downward (i.e., Ch-type asteroid) or convex upward (i.e., non-Ch-type asteroid) near $0.7 \mu\text{m}$. Such discrepancy could be caused by the rotational spectral variation (Hasegawa et al. 2024), the different observation circumstances, or an artifact associated with the observations or data analysis process. We confirmed that the wider bandwidth of ECAS (v-, x-, and w-bands' FWHMs are $0.06\text{--}0.08 \mu\text{m}$, Zellner et al. 1985) is not responsible for these discrepancies. To avoid the uncertainty arising from the discrepancies in $\hat{R}_{0.7}$ values, we only used the asteroids when their $\hat{R}_{0.7}$ values from the different references are consistent with each other within their uncertainties. This selection process excluded $\hat{R}_{0.7}$ data of 21 asteroids: (13) Egeria, (35) Leukothea, (50) Virginia, (52) Europa, (54) Alexandra, (56) Melete, (62) Erato, (65) Cybele, (88) Thisbe, (93) Minerva, (99) Dike, (130) Elektra, (209) Dido, (233) Asteroppe, (238) Hypatia, (266) Aline, (386) Siegena, (515) Athalia, (559) Nanon, (704) Interamnia, and (804) Hispania.

Regarding the $2.7 \mu\text{m}$ band, we used data from the Asteroid Catalog using AKARI (AcuA, Usui et al. 2019). The AcuA provides $2.7 \mu\text{m}$ band depths, taking advantage of the space observatory (i.e., an infrared astronomy satellite developed and operated by Japan Aerospace Exploration Agency, AKARI), which allows us to avoid significant influence by telluric absorption (Rivkin et al. 2000). To characterize the $2.7 \mu\text{m}$ bands, we modified the $2.7 \mu\text{m}$ band depth values ($\mathcal{D}_{2.7}$) from Table 5 in Usui et al. (2019) using the equation given by

$$\hat{R}_{2.7} = (100 - \mathcal{D}_{2.7})/100, \quad (5)$$

where $\mathcal{D}_{2.7}$ is given in percent. We use $\hat{R}_{2.7}$ as the index representing the $2.7 \mu\text{m}$ band depth. To increase the sample size, we used absorption depths measured at $2.9 \mu\text{m}$ from Takir & Emery (2012); Takir et al. (2015) for eight asteroids. Note that Takir & Emery (2012); Takir et al. (2015) derived the $2.9 \mu\text{m}$ band depth (not $2.7 \mu\text{m}$). Because Takir & Emery (2012); Takir et al.

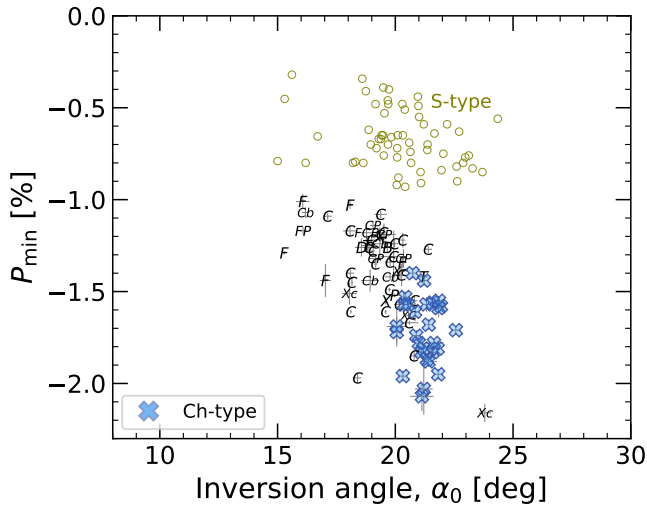


Fig. 2. Relationship between P_{\min} and α_0 for dark asteroids. Markers indicate the asteroids’ spectral type based on Tholen, SMASSII, or Bus-DeMeo classifications (Tholen 1984; Bus & Binzel 2002; Lazzaro et al. 2004; DeMeo et al. 2009; Hasegawa et al. 2024). The cross markers represent asteroids classified as Ch-types in previous studies (Bus & Binzel 2002; Lazzaro et al. 2004; DeMeo et al. 2009; Hasegawa et al. 2024). Only P_{\min} values fitted with sufficient data points (three or more data points near α_{\min} , i.e., $5 < \alpha < 15$) are plotted. The empty circles show the S-type asteroids for the comparison (Gil-Hutton, R. & García-Migani, E. 2017; Lupishko 2019; Bendjoya et al. 2022).

(2015) conducted the ground-based observations, the $2.7\mu\text{m}$ range could not be observed due to serious telluric absorption. Despite the different definitions of band depth between Usui et al. (2019) and other two papers (Takir & Emery 2012; Takir et al. 2015), we used the $2.9\mu\text{m}$ band depth from Takir et al. (2015) as a proxy of the $2.7\mu\text{m}$ band depth for eight asteroids to increase the number of samples. These 14 asteroids are (34) Circe, (36) Atalante, (41) Daphne, (48) Doris, (54) Alexandra, (76) Freia, (91) Aegina, (98) Ianche, (104) Klymene, (107) Camilla, (190) Ismene, (31) Euphrosyne, (324) Bamberg, and (334) Chicago. These data points are marked with the different markers in Fig. 3.

3. Results

In total, we obtained polarimetric properties of 199 dark asteroids by compiling polarimetric data from both our observations and previous research (Cellino et al. 2015; Gil-Hutton, R. & García-Migani, E. 2017; Devogèle et al. 2017; Belskaya et al. 2017; Lupishko 2018; López-Sisterna et al. 2019; Bendjoya et al. 2022; Kwon et al. 2023). Notably, the sample size of asteroids classified as Ch-type (Bus & Binzel 2002; Lazzaro et al. 2004; DeMeo et al. 2009; Hasegawa et al. 2024) has increased from 9 to 67, representing a sevenfold growth compared to those in Belskaya et al. (2017). Following Belskaya et al. (2017), we compare P_{\min} and α_0 in Fig. 2 and confirm the distinctive P_{\min} values for all observed Ch-type asteroids. The nightly weighted mean values of the polarimetric result obtained from our observations are summarized in Tables D1, and PPC plots are given in Figs. D3. The polarimetric parameters obtained or updated in this study are summarized in Table 1. Hereafter, we describe our findings by comparing spectral and photometric properties.

3.1. Correlation between polarimetric and spectral properties

In Fig. 3, we compare the NPB properties (P_{\min} , h , α_0 , and α_{\min}) of dark asteroids with their spectral properties related to the hydrated minerals (\hat{R}_{UV} , $\hat{R}_{0.7}$, and $\hat{R}_{2.7}$). In these plots, we regard asteroids with $\hat{R}_{0.7}$ +their $1-\sigma$ uncertainties ($\sigma\hat{R}_{0.7}$) < 1 as Ch-types (the cross marker in Fig. 3). Accordingly, all Ch-type asteroids distribute below the line of $\hat{R}_{0.7} = 1$. Since Ch-type asteroids are generally regarded as strongly hydrated asteroids, they exhibit small \hat{R}_{UV} and $\hat{R}_{2.7}$ values. As we described in Sect. 1, Belskaya et al. (2017) noticed that Ch-type asteroids are distinctive in that they exhibit deep NPBs (that is, large $|P_{\min}|$ values). In Fig. 3a–c, the majority of Ch-type asteroids have NPBs ($|P_{\min}| \gtrsim 1.5\%$) deeper than other taxonomic types, which is consistent with Belskaya et al. (2017). In addition, due to the increased sample size, the correlations between P_{\min} and spectral properties (\hat{R}_{UV} , $\hat{R}_{0.7}$, and $\hat{R}_{2.7}$) associated with the hydrated minerals are clearly seen in Fig. 3a–c. Other polarization properties (h , α_0 , and α_{\min}) also appear to correlate with these three spectral properties related to hydrated minerals.

To quantify these correlations, we measured the Spearman correlation coefficients (ρ) and their $1-\sigma$ uncertainties (σ_ρ) using the following procedure. We employed the Monte Carlo simulation with 10 000 iterations. In each iteration, we randomized the data by adding Gaussian noises with their measurement uncertainties and computed the Spearman coefficients, ρ_i . Then, we took the median and the half of the central 68% interval of the distribution of ρ_i as ρ and σ_ρ . To derive the correlation coefficients, we used only the asteroid samples whose P_{\min} , h , and α_0 are all available. The sample size of asteroids to derive ρ are 49, 69, and 19 for \hat{R}_{UV} , $\hat{R}_{0.7}$, and $\hat{R}_{2.7}$, respectively. The obtained values of ρ and σ_ρ are summarized in Table 2 and shown in Fig. 3.

We find that in the majority of cases (10 out of 12), there are moderately good linear correlations between NPB properties and spectral features related to hydrated minerals, with $\rho > 0.4$. Notably, $\hat{R}_{UV}-P_{\min}$ and $\hat{R}_{UV}-\alpha_0$ show the strong correlations, with $\rho > 0.6$. Two combinations, $\hat{R}_{2.7}-\alpha_0$ and $\hat{R}_{2.7}-\alpha_{\min}$, show the weak correlations with $\rho < 0.3$. However, in Fig. 3b, there are non-Ch-type asteroids that exhibit the large $|P_{\min}|$ ($> 1.5\%$) values but distribute on or above the line of $\hat{R}_{0.7} = 1$ (the area enclosed by the orange rectangle). These asteroids are (1) Ceres, (24) Themis, (46) Hestia, (96) Aegle, (222) Lucia, (398) Admete, (409) Aspasia, (476) Hedwig, and (511) Davida. Moreover, on the upper right edge of Fig. 3a, there is one outlier, (213) Lillaea ($P_{\min} = -1.97 \pm 0.03\%$ and $\hat{R}_{UV} = 1.06 \pm 0.03$, the taxonomy type of F- and B-type). We will discuss these asteroids in Sect. 4.

3.2. Correlation between polarimetric and photometric properties

To examine the photometric properties of asteroids, we analyzed the photometric phase curves (PhotPC). The PhotPC is the profile describing how the disk-integrated brightness of an asteroid changes with α (Bowell et al. 1989). The PhotPC provides information on the light-scattering characteristics of the asteroid surface, which would be linked to their regolith composition and structures (Muinonen et al. 2022). The PhotPC at low phase angles can be characterized by two parameters: the slope of the curve and the amplitude associated with the opposition effect (OE). The OE is the sharp increase in asteroid brightness that occurs when α approaches zero. For the comparison, we adopted the OE amplitude measured at $\alpha = 0.3^\circ$ ($\text{OE}_{0.3^\circ}$) and

Table 1. Summary of key polarimetric parameters

Target	Taxonomy ^a	P_{\min}^b (%)	α_{\min}^b (deg)	h^b (%/deg)	α_0^b (deg)	Ref _{SM} ^c	Ref _{BD} ^d
(19) Fortuna	G/Ch/Ch	-1.83 ± 0.02	8.93 ± 0.11	0.241 ± 0.009	21.59 ± 0.14	(1)	(4)
(24) Themis	C/B/C	-1.57 ± 0.04	10.00 ± 0.12	0.308 ± 0.011	20.17 ± 0.22	(1)	(4)
(41) Daphne	C/Ch/Ch	-1.74 ± 0.03	9.89 ± 0.26	0.301 ± 0.007	20.89 ± 0.13	(1)	(4)
(49) Pales	CG/Ch/Ch	-1.87 ± 0.03	9.31 ± 0.22	0.304 ± 0.012	21.34 ± 0.13	(1)	(4)
(54) Alexandra	C/C/Cgh	-1.95 ± 0.03	10.46 ± 0.36	0.324 ± 0.017	21.82 ± 0.18	(1)	(4, 6)
(58) Concordia	C/Ch/Ch	-1.88 ± 0.03	10.57 ± 0.19	...	21.41 ± 0.37	(1)	(4)
(66) Maja	C/Ch/Ch	-1.81 ± 0.04	10.80 ± 0.14	0.323 ± 0.011	21.80 ± 0.16	(1)	(4)
(70) Panopaea	C/Ch/Cgh	-1.81 ± 0.05	10.06 ± 0.13	0.348 ± 0.015	20.27 ± 0.17	(1)	(4, 6)
(91) Aegina	CP/Ch/Ch	-1.56 ± 0.02	10.71 ± 0.09	0.283 ± 0.008	21.59 ± 0.14	(1)	(5)
(95) Arethusa	C/Ch/Ch	0.316 ± 0.010	21.06 ± 0.14	(1)	(5)
(99) Dike	C/Xk/Xc	-2.16 ± 0.05	11.80 ± 0.14	0.355 ± 0.010	23.80 ± 0.26	(1)	(6)
(105) Artemis	C/Ch/Ch	-1.57 ± 0.07	...	0.268 ± 0.003	20.36 ± 0.15	(1)	(4)
(111) Ate	C/Ch/Ch	0.310 ± 0.021	20.92 ± 0.24	(1)	(6)
(128) Nemesis	C/C/C	-1.49 ± 0.01	9.25 ± 0.22	0.264 ± 0.009	19.75 ± 0.07	(1)	(4,6)
(142) Polana	F/B/C	-1.06 ± 0.04	8.20 ± 0.15	0.248 ± 0.009	16.56 ± 0.15	(1)	(6)
(144) Vibilia	C/Ch/Cgh	-1.70 ± 0.05	10.43 ± 0.12	0.318 ± 0.008	21.01 ± 0.15	(1)	(5,6)
(147) Protogeneia	C/C/C	-0.99 ± 0.11	10.19 ± 0.89	(1)	(4)
(162) Laurentia	STU/Ch/Ch	-1.55 ± 0.04	10.34 ± 0.76	(1)	(6)
(173) Ino	C/Xk/Xc	-1.33 ± 0.14	9.51 ± 0.80	0.250 ± 0.019	19.29 ± 0.66	(1)	(7)
(176) Iduna	G/Ch/Ch	-1.87 ± 0.08	(1)	(6)
(207) Hedda	C/Ch/Ch	-1.58 ± 0.03	10.71 ± 0.26	(1)	(5)
(209) Dido	C/X/C	-1.11 ± 0.09*	(1)	(6)
(233) Asterope	T/K/Xk	(1)	(4)
(238) Hypatia	C/Ch/...	-1.59 ± 0.05	10.82 ± 0.12	...	21.84 ± 0.24	(1)	...
(240) Vanadis	C/C/Cgh	-1.57 ± 0.06	11.36 ± 0.46	(1)	(5)
(257) Silesia	SCTU/Ch/...	-1.66 ± 0.07	11.79 ± 1.05	(1)	...
(266) Aline	C/Ch/Ch	-1.51 ± 0.04	11.40 ± 0.78	(1)	(4, 5, 6)
(282) Clorinde	BFU::/B/C	-1.04 ± 0.09	8.47 ± 0.17	0.248 ± 0.026	17.07 ± 0.34	(1)	(11)
(284) Amalia	CX/Ch/Ch	-1.48 ± 0.07	...	0.274 ± 0.009	21.09 ± 0.12	(1)	(1)
(308) Polyxo	T/T/T	-1.42 ± 0.02	10.53 ± 0.07	0.266 ± 0.005	21.21 ± 0.17	(1)	(4)
(357) Ninina	CX/B/Ch	-1.53 ± 0.05	11.48 ± 0.51	(2)	(8)
(368) Haidea	D/D/D	-1.26 ± 0.05	9.19 ± 0.18	0.264 ± 0.011	18.56 ± 0.28	(3)	(3)
(375) Ursula	C/Xc/C	-1.18 ± 0.05	9.94 ± 0.41	(1)	(6)
(398) Admete	.../C/Cg	-1.55 ± 0.13	(1)	(6)
(405) Thia	C/Ch/Ch	-1.55 ± 0.02	10.86 ± 0.11	0.279 ± 0.004	21.85 ± 0.14	(1)	(5)
(410) Chloris	C/Ch/Ch	0.312 ± 0.010	21.25 ± 0.17	(1)	(5)
(442) Eichsfeldia	C/Ch/B	-1.54 ± 0.06*	(1)	(9)
(490) Veritas	C/Ch/Ch	-1.60 ± 0.05	11.22 ± 0.50	(1)	(12)
(503) Evelyn	XC/Ch/...	-1.62 ± 0.04	10.63 ± 0.07	0.297 ± 0.010	21.42 ± 0.15	(1)	...
(586) Thekla	C:/Ch/Ch	-1.70 ± 0.13	(1)	(5)
(602) Marianna	C/Ch/...	-1.72 ± 0.09	12.81 ± 1.10	(2)	...
(618) Elfriede	C/C/...	-1.36 ± 0.17*	(2)	...
(771) Libera	X/X/Xk	-1.14 ± 0.17*	(1)	(13)
(776) Berbericia	C/Cgh/Cgh	-1.78 ± 0.02	10.68 ± 0.20	0.323 ± 0.009	21.64 ± 0.40	(1)	(4,5)
(821) Fanny	C/Ch/...	-1.25 ± 0.16*	(1)	...
(1015) Christa	C/Xc/C	-1.15 ± 0.10*	(1)	(6)
(1201) Strenua	.../Xc/...	-0.92 ± 0.27	(1)	...
(1542) Schalen	.../D/D	-1.07 ± 0.08*	(1)	(4)
(1754) Cunningham	P/X/...	-0.94 ± 0.16*	(2)	...
(1795) Woltjer	.../Ch/B	-2.40 ± 0.30*	(1)	(5)
(2569) Madeline	.../D/...	-1.29 ± 0.07*	(1)	...

Notes. Asteroids whose polarimetric parameters are newly reported or updated by this study are shown. ^(a) Taxonomy type based on Tholen (Tholen 1984), SMASSII (Bus 1999; Bus & Binzel 2002) and Bus-DeMeo (DeMeo et al. 2009) classifications, respectively. All Tholen taxonomy types are from Tholen (1984), ^(b) Polarimetric parameters derived in this study ^(c) Reference of the SMASSII taxonomy, ^(d) Reference of the Bus-DeMeo taxonomy, ^(*) P_r taken at $8^\circ < \alpha < 12^\circ$ is used as the proxy of P_{\min} . The table contents are available via <http://cdsarc.u-strasbg.fr/viz-bin/cat/J/A+A/XXX/XXX>.

References. (1) Bus & Binzel (2002); (2) Lazzaro et al. (2004); (3) Gartelle et al. (2021); (4) DeMeo et al. (2009); (5) Vernazza et al. (2016); (6) Hasegawa et al. (2024); (7) DeMeo et al. (2022); (8) de León et al. (2012); (9) Reddy & Sanchez (2016); (10) Clark et al. (2004); (11) Arredondo et al. (2021); (12) Ziffer et al. (2011); (13) Neeley et al. (2014)

Table 2. Spearman correlation coefficients

	P_{\min}		h		α_0		α_{\min}	
	ρ	σ_ρ	ρ	σ_ρ	ρ	σ_ρ	ρ	σ_ρ
\hat{R}_{UV}	-0.67	0.03	-0.43	0.05	-0.64	0.04	-0.40	0.04
$\hat{R}_{0.7}$	-0.58	0.04	-0.55	0.05	-0.47	0.04	-0.37	0.05
$\hat{R}_{2.7}$	-0.54	0.14	-0.42	0.13	-0.29	0.13	-0.03	0.13
$OE_{0.3^\circ}$	0.81	0.07	0.47	0.09	0.38	0.06	0.22	0.10
b	-0.70	0.06	-0.52	0.08	-0.58	0.06	-0.58	0.09

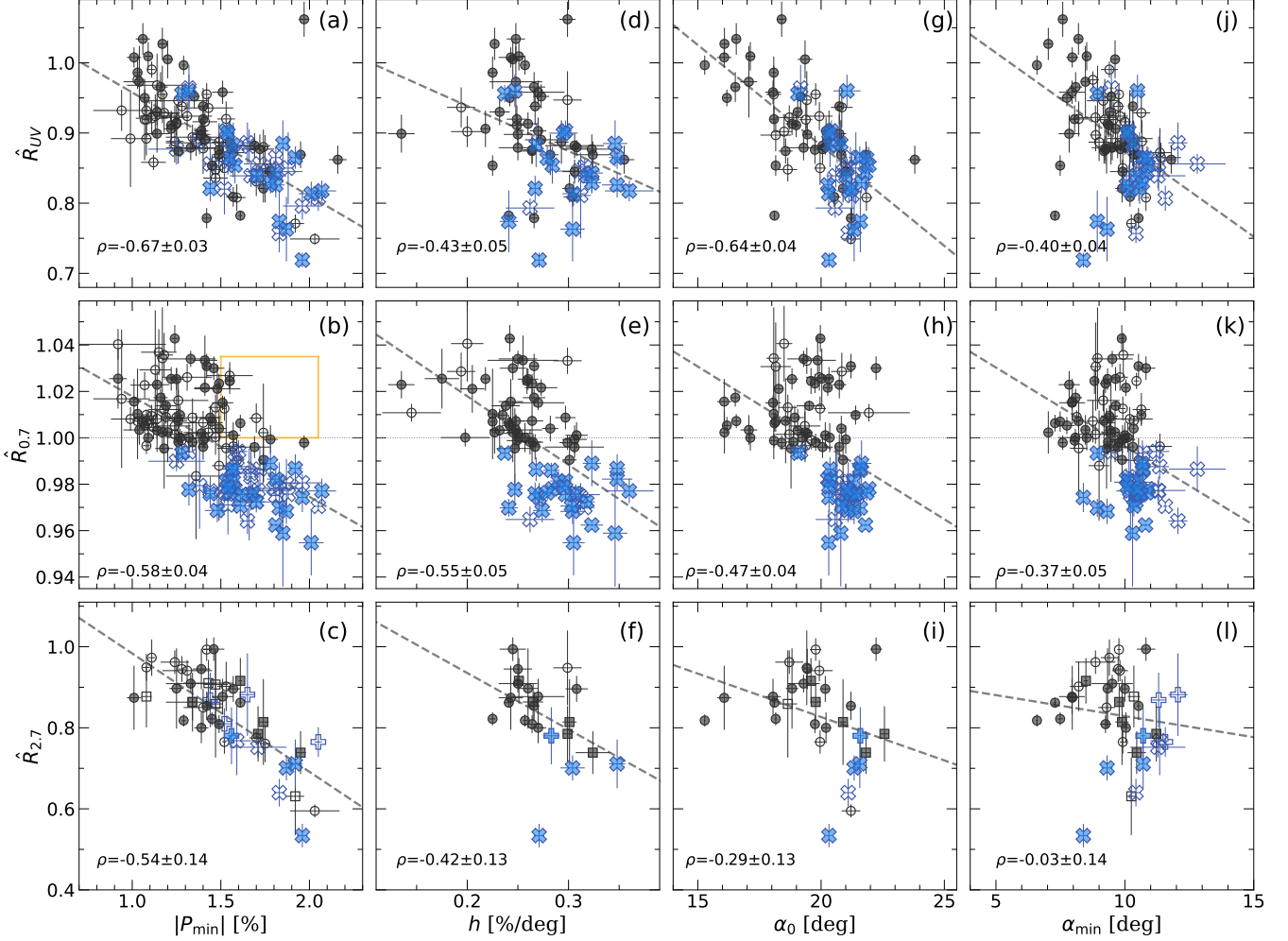


Fig. 3. Comparison between the polarimetric properties (P_{\min} , h , α_0 and α_{\min}) of dark asteroids and their spectral properties associated with the hydrated minerals (\hat{R}_{UV} , $\hat{R}_{0.7}$, and $\hat{R}_{2.7}$). Blue cross markers indicate asteroids with $R_{0.7} + \sigma R_{0.7} < 1$ (i.e., Ch-type asteroids, DeMeo et al. 2009), while black circles indicate dark asteroids other than Ch-type. The filled markers mean the asteroids whose P_{\min} , h , and α_0 are all obtained. The empty markers indicate asteroids with only one parameter out of three reported. The dashed lines are the linear lines fitted by using filled markers. In panel (b), the orange square encloses the asteroids that have the large $|P_{\min}|$ ($> 1.5\%$) values but distribute on or above the line of $\hat{R}_{0.7} = 1$. In panels (c), (f), (i), and (l), $\hat{R}_{2.7}$ values from Takir & Emery (2012); Takir et al. (2015) are represented as plus and square markers for Ch-type and other type asteroids, respectively.

the slope of the linear part of the phase curve (b) in the V -band from four sources: Belskaya & Shevchenko (2000); Shevchenko et al. (2002, 2008, 2012). For the data in Shevchenko et al. (2008, 2012), we derived b values using the reduced magnitude ($V_0(1, \alpha)$) in the references, following the b measurement method in Belskaya & Shevchenko (2000). Then, we used these b values for comparison. These photometric properties ($OE_{0.3^\circ}$ and b) are compared with NPBs and spectral properties for 18 asteroids: (10) Hygiea, (24) Themis, (47) Aglaja, (50) Virginia, (59) Elpis, (76) Freia, (91) Aegina, (102) Miriam, (105) Artemis,

(127) Johanna, (130) Elektra, (146) Lucina, (165) Loreley, (190) Ismene, (211) Isolda, (313) Chaldaea, (419) Aurelia, and (588) Achilles. We computed ρ and σ_ρ values using the same method as described in Sect. 3.1 and summarized in Table 2. The comparison is shown in Fig. 4.

In Fig. 4a–d and h–k, most combinations (6 out of 8) between NPBs and photometric properties show moderate correlations ($\rho > 0.4$). The weak correlation is seen in the $OE_{0.3^\circ}$ – α_{\min} plot, with $\rho = 0.22 \pm 0.10$. Notably, $OE_{0.3^\circ}$ – P_{\min} shows the strongest linear correlation, with $\rho = 0.81 \pm 0.07$. As well as the

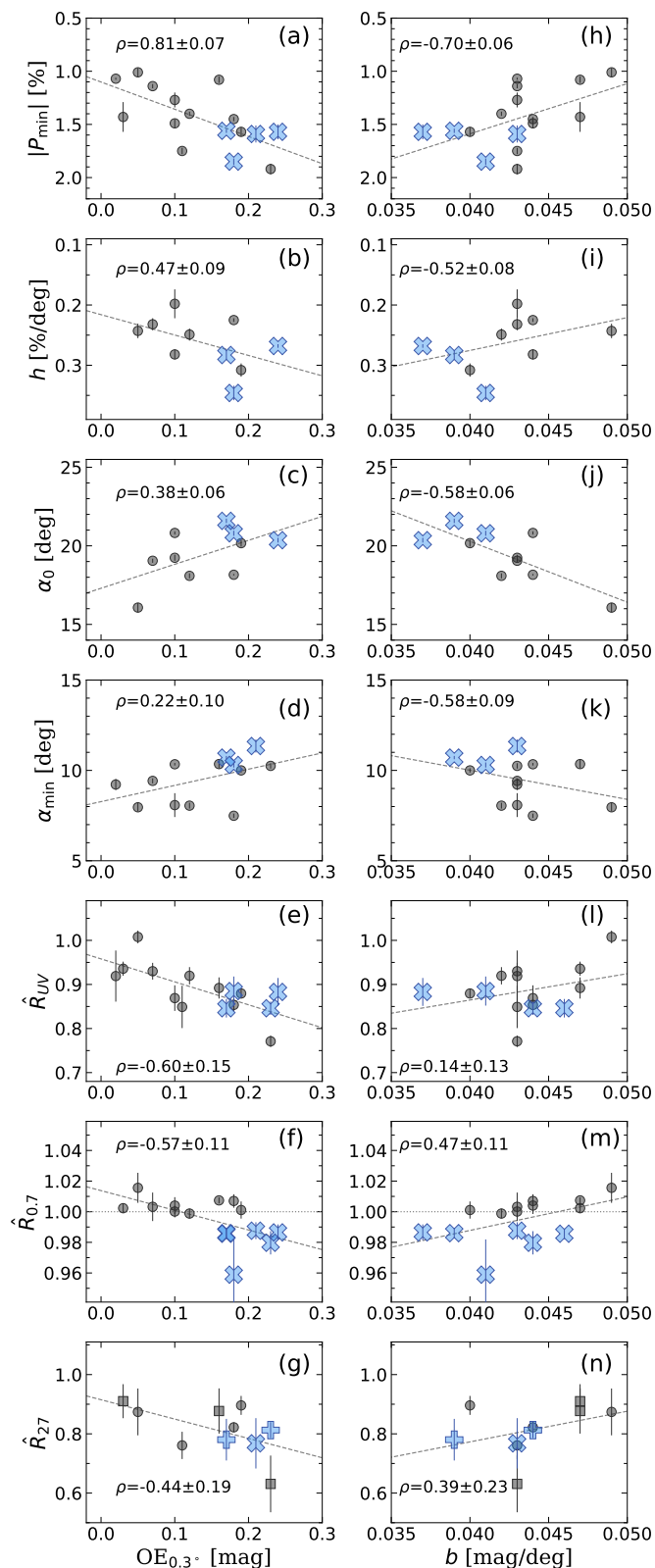


Fig. 4. Comparison of the photometric properties (i.e., $OE_{0.3^\circ}$ and b) with the polarimetric (P_{\min} , h , α_0 and α_{\min}) and spectral (\hat{R}_{UV} , $\hat{R}_{0.7}$, and $\hat{R}_{2.7}$) properties of dark asteroids. Blue cross markers indicate asteroids with $\hat{R}_{0.7} + \sigma\hat{R}_{0.7} < 1$ (i.e., Ch-type asteroids, DeMeo et al. 2009), while black circles indicate dark asteroids other than the Ch-type. In panels (g) and (n), plus and square markers represent $\hat{R}_{2.7}$ values from Takir & Emery (2012); Takir et al. (2015) for Ch-type and other type asteroids, respectively.

NPB properties, the most spectral properties associated with the hydrated minerals (\hat{R}_{UV} , $\hat{R}_{0.7}$, and $\hat{R}_{2.7}$) also show moderate correlations ($\rho > 0.4$) with the photometric properties. Especially, $OE_{0.3^\circ}$ shows good correlations with all spectral features as their $\rho > 0.4$. Only the combination of \hat{R}_{UV-b} shows the weak correlation as its $\rho = 0.14 \pm 0.13$.

The Fig. 4 includes six Ch-type asteroids (i.e., (91) Aegina, (105) Artemis, (127) Johanna, (146) Lucina, (211) Isolda, and (313) Chaldaea). It is noteworthy that Ch-type asteroids not only have larger $|P_{\min}|$ values ($> 1.5\%$ in Fig. 4a) but also show a stronger opposition effect than other dark asteroids. In Fig. 4a–g, all Ch-types asteroids fall into the range of $OE_{0.3^\circ} > 0.17$ mag, indicating the notably larger OE than other dark asteroids. In contrast, b values for Ch-type asteroids span a relatively wide range. In Fig. 4m, the b values for Ch-type asteroids range from 0.037 to 0.046 mag deg $^{-1}$, which is similar to other dark asteroids (0.037–0.049 mag deg $^{-1}$).

4. Discussion

4.1. Asteroids with deep NPBs and associated meteorites

There are two major types of hydrated meteorites: CM- and CI-type carbonaceous meteorites. The spectral characteristics of CM-type meteorites include the $0.7\mu\text{m}$ band associated with Fe^{2+} – Fe^{3+} charge transfer in Fe-rich phyllosilicate (Gaffey & McCord 1979; Vilas & Gaffey 1989), the $2.7\mu\text{m}$ band associated with OH incorporated into phyllosilicates (Rivkin et al. 2002), and the UV drop-off caused by a ferric oxide intervalence charge transfer transition (Vilas 1994). On the other hand, CI-meteorites generally exhibit weaker (or no) $0.7\mu\text{m}$ absorption than CM-type meteorites, although the other spectral properties of UV drop-off and the $2.7\mu\text{m}$ band absorption are similar to CM-type meteorites (Takir et al. 2013). Because of the spectral similarity, Ch-type asteroids are occasionally linked with CM-like asteroids. Following this fact, we refer to asteroids with hydration signatures of the $2.7\mu\text{m}$ bands and the UV drop-off but without the $0.7\mu\text{m}$ band as CI-like asteroids. Note that the definition of CI-like asteroids in this study is observation-based, so CI-like asteroids do not necessarily have the mineral composition of CI meteorites. Vilas (1994) argued that asteroids with hydration signatures of the $2.7\mu\text{m}$ band but without the $0.7\mu\text{m}$ band could be due to a lack of oxidized iron in the hydrated minerals. This could be explained by the iron-poor composition: the depletion of Fe^{2+} due to conversion to Fe^{3+} , or the mild heating ($400^\circ\text{C} < T < 600^\circ\text{C}$, Hiroi et al. 1993) that these asteroids may have undergone after the aqueous alteration (Fornasier et al. 2014).

Belskaya et al. (2017) noticed that Ch-type asteroids (CM-like asteroids) have distinctively deep P_{\min} compared to other dark asteroids. We also confirmed this distinctive polarimetric property of Ch-type. However, it is important to note that 10 asteroids that are not classified as Ch-type (hereafter, non-Ch-type) have deep P_{\min} values (see Fig. 3b, the asteroid enclosed by the orange rectangle). These 11 asteroids consist of (1) Ceres, (24) Themis, (46) Hestia, (96) Aegle, (194) Prokne, (213) Lilaea, (222) Lucia, (398) Admete, (409) Aspasia, (476) Hedwig, and (511) Davida. We examine the spectral and orbital properties of these asteroids and find that most of them (8 out of 11) have evidence for hydration. The near-IR spectra of six asteroids ((1) Ceres, (24) Themis, (46) Hestia, (96) Aegle, (476) Hedwig, and (511) Davida) indicate the signature of hydrated minerals on their surfaces (i.e., $\hat{R}_{2.7} < 1$, Usui et al. 2019; Kwon et al. 2022). Additionally, the mid-IR spectrum of (194) Prokne provided evi-

dence of its hydration (McAdam 2017). We cannot confirm a hydration feature of (222) Lucia due to no available spectral data at $2.7\ \mu\text{m}$. However, because this asteroid is dynamically classified in the Themis collisional family (the analog meteorite is likely the hydrated one, Clark et al. 2010), we suspect that (222) Lucia is an asteroid with hydrated minerals. The hydration state of (398) Admete and (409) Aspasia cannot be confirmed due to the lack of their spectral data around UV and $2.7\ \mu\text{m}$ wavelength. Only (213) Lilaea has neither $0.7\ \mu\text{m}$ band nor UV bands. Since there is no spectral data around the $2.7\ \mu\text{m}$ wavelength, it remains unclear whether (213) Lilaea is the hydrated asteroid. Although we cannot confirm the hydration status of three out of 10 asteroids, we note that most of the 10 non-Ch-asteroids with evidence of hydration (i.e., CI-like asteroids) have large P_{\min} values. The deep P_{\min} of CI-like asteroids can also be found from the previous studies. Gil-Hutton & Cañada-Assandri (2012) analyzed 39 C-complex asteroids to derive the mean polarimetric parameters for different subsets within the C-complex. They reported the mean P_{\min} values of $-1.57 \pm 0.15\%$ for Ch-types and $-1.69 \pm 0.12\%$ for C-types asteroids, indicating that C-type asteroids have deeper NPBs than Ch-types. However, we found that most of the C-type asteroids used to derive the mean value are CI-like asteroids, which is consistent with our findings. Therefore, we consider that not only CM-like asteroids but also the asteroids without or weak $0.7\ \mu\text{m}$ band absorption (i.e., CI-like asteroids) would have large P_{\min} values.

This fact matches the laboratory measurements of meteoric samples. Zellner et al. (1977) (in Table 4 and 5 in the reference) obtained the NPBs of the carbonaceous meteorites, including CM-, CI-, CV-, and CO-type meteorites in the O - and G -bands (the central wavelengths of $0.585\ (O)$ and $0.520\ \mu\text{m}\ (G)$, respectively). They crushed the meteorite samples without grounding or sieving to make a mixture of broad particle size range ($< 500\ \mu\text{m}$). They created a roughness of these samples with a needle. Later, Geake & Dollfus (1986) (Table 4 in the reference) measured the NPBs of CM-, CI-, CV-, and CK-type meteorites in $0.58\ \mu\text{m}$ wavelength. These samples were powdered (the size range of $20\text{--}340\ \mu\text{m}$). All analyzed carbonaceous meteorites are dark with $p_{V,5^\circ} \lesssim 0.1$. Here, $p_{V,5^\circ}$ is the albedo at $\alpha = 5^\circ$. The names of the analyzed meteorites are summarized in Ishiguro et al. (2022). As a result, Zellner et al. (1977) and Geake & Dollfus (1986) found that CM- and CI-type meteorites have the deep NPBs ($|P_{\min}| > 1.5\%$), while CO-, CV-, and CK-type meteorites have the shallow NPBs ($|P_{\min}| < 1.5\%$). To summarize the above discussion, not only Ch-type asteroids (linked with CM meteorites) but also some dark asteroids (non-Ch-type asteroids, which are linked with CI meteorites) are likely to exhibit the deep $|P_{\min}|$ values in NPBs.

4.2. Possible surface properties of hydrated asteroids

As we mentioned above, both observational and laboratory evidence show that hydrated asteroids and meteorites have deep NPBs. Furthermore, we demonstrated the clear correlations between the NPB parameters and the spectral features associated with their hydration (i.e., \hat{R}_{UV} , $\hat{R}_{0.7}$, and $\hat{R}_{2.7}$). The NPB properties are determined by not only the surface composition but also the surface texture, such as the size parameters, porosity, or microtexture (Dollfus & Geake 1977; Geake & Geake 1990; Belskaya et al. 2017; Gil-Hutton, R. & García-Migani, E. 2017; Spadaccia et al. 2022; Bach et al. 2024a). Here, we refer to microtexture as the microscopic roughness, size, and shape created by minerals on the grain surfaces. In the following subsections, we discuss a few possible mechanisms why hy-

drated (i.e., CM- and CI-like) asteroids have deep NPBs from various aspects.

4.2.1. Geometric albedo

The geometric albedo at the V -band (p_V) is one of the key properties that affect the polarization degree of asteroids (Umov 1905; Dollfus & Geake 1977; Geake & Dollfus 1986; Cellino et al. 2015). It is reported that low p_V asteroids exhibit deep NPBs along with large values of h and $|P_{\min}|$ (Cellino et al. 2015). Due to the tight correlation between h and p_V (Widorn 1967; Cellino et al. 2015; Lupishko 2018), h is regarded as a proxy of p_V and is used to obtain p_V of small Solar System bodies (e.g., Cellino et al. 2005; Geem et al. 2022b, 2023).

To investigate if the p_V influences the deep NPBs of the hydrated asteroids, we compared their polarimetric and spectral features with their p_V values. In Fig. 5, we utilized the p_V values derived based on the stellar occultation with photometric data (p_{V^*} , Shevchenko & Tedesco 2006; Lupishko 2018). These albedo values (p_{V^*}) are regarded as reliable ones obtained through ground-based observations (Tedesco 1994). From Fig. 5, we cannot find clear correlations ($\rho \leq 0.3$) for all combinations but one. Only $\hat{R}_{2.7}$ shows a moderate correlation with p_{V^*} (Fig. 5g, $\rho = -0.40 \pm 0.11$). It should be emphasized that h shows a negligible correlation with p_{V^*} (see Fig. 5b, $\rho = -0.10 \pm 0.08$), suggesting that p_V is not the primary factor contributing to the deep NPBs in hydrated asteroids. However, it is likely that the relation between p_V and NPBs may not work for low p_V asteroids because the relation between h and p_V breaks down (often referred to as ‘saturation’ in reference papers) for dark asteroids ($p_V \lesssim 0.05$, Geake & Dollfus 1986; Bach et al. 2024a). We conjecture that the relation between P_{\min} and p_V also breaks down similarly to h and p_V relation. From the weak correlation between P_{\min} and p_V , we consider that the albedo is not the main mechanism for the deep NPB of hydrated asteroids.

4.2.2. Surface texture

Many efforts in light-scattering measurements in laboratories have been conducted to examine the relationship between NPBs and surface texture properties (e.g., size parameters, porosity, and the microtexture, Dollfus & Geake 1977; Geake et al. 1984; Dollfus 1998; Geake & Geake 1990; Shkuratov et al. 2006). For example, Dollfus & Geake (1977) investigated the NPBs of three different lunar samples: lunar fines, lunar rock chips with some adhering dust, and lunar rock chips clean of dust. They found that lunar fines exhibited the deepest NPBs with the large $|P_{\min}|$ and α_0 , while the dust-free rocks showed the shallowest NPBs among the three samples. This result implies that the surface textures influence NPBs. Later, Geake & Geake (1990) examined how the grain size parameter affects the NPBs. They measured the NPBs of the sample with the sizes of $0.05, 0.3, 1, 4, 12,$ and $40\ \mu\text{m}$ at $0.535\ \mu\text{m}$ wavelength. Although they used the term ‘grain size’, the authors clarified that the three finer samples’ grain sizes (i.e., $0.05, 0.3,$ and $1\ \mu\text{m}$) refer to crystal sizes responsible for the surface roughness of each grain particle (i.e., microtexture). From this experiment, Geake & Geake (1990) noticed that the depth of NPBs is significantly enhanced, with large $|P_{\min}|$ values when grain size approaches or falls below the wavelength scale. They further found that α_0 also varies when the grain size is similar to or smaller than the wavelength, with α_0 values becoming maximum when the sample grain size is twice the wavelength. Shkuratov et al. (2006) independently measured

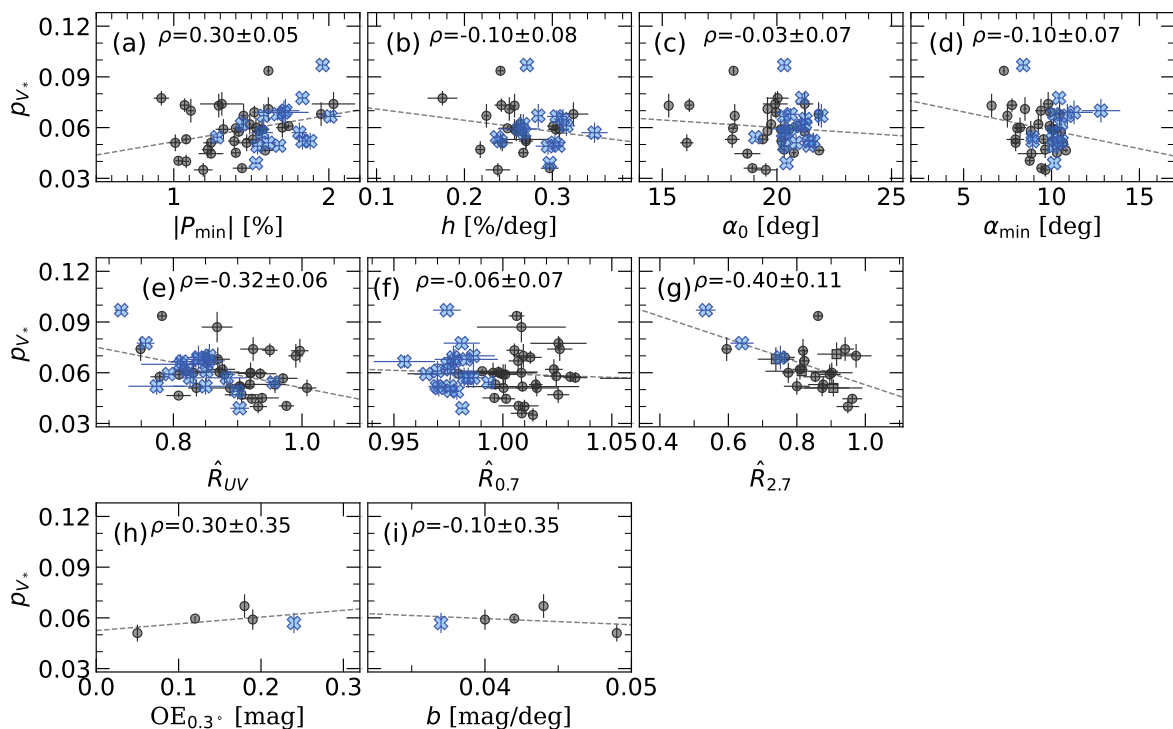


Fig. 5. Comparison between the geometric albedo derived by the stellar occultation (p_{V^*} , Shevchenko & Tedesco 2006; Lupishko 2018), the polarimetric, photometric properties and spectral properties associated with the low albedo asteroids with hydration features. Blue cross markers indicate asteroids with $\hat{R}_{0.7} + \sigma\hat{R}_{0.7} < 1$ (i.e., Ch-type asteroids, DeMeo et al. 2009), while black circles indicate dark asteroids other than Ch-type. (g) Square markers indicate the asteroids whose $\hat{R}_{2.7}$ are obtained from Takir & Emery (2012); Takir et al. (2015).

the NPBs of olivine samples with different sizes (1.3, 2.6, and 3.8 μm) at the wavelength of 0.63 and 0.45 μm and found deeper NPBs for the smaller grain sample.

According to previous laboratory research (Dollfus & Geake 1977; Geake & Geake 1990; Shkuratov et al. 2006), there is a trend that the observed NPBs get deeper when the surface textures scale that mainly affect the observed polarimetric properties become comparable to or smaller than the wavelength. On the other hand, Belskaya et al. (2017) and Kwon et al. (2023) suggested that Ch-type asteroids have a larger $|P_{\min}|$ and α_0 than other types F, B, P, and T-type of dark asteroids. In Sect. 3.1, we found the correlations between the polarimetric properties (P_{\min} and α_0) and the spectral properties associated with the hydrated minerals (see Fig. 3a–c and g–i). Both laboratory experiments, previous observational results, and our findings may imply that one of the main contributors to the deep NPBs of hydrated asteroids could be surface structures with length scales comparable to or smaller than the optical wavelengths (i.e., submicrometer-sized textures).

One of the possible submicrometer-sized textures found on the hydrated asteroids could be the microtexture of phyllosilicates. Phyllosilicates are considered the dominant minerals in hydrated asteroids. CM- and CI-type meteorites, believed to originate from hydrated asteroids, contain phyllosilicates as their primary mineral: phyllosilicates comprise 73–79 % of the mass in CM-type meteorites (Howard et al. 2009) and 81–84 % of the mass in CI-type meteorites (King et al. 2015). In contrast, other carbonaceous chondrites, such as CV- and CO-type me-

teorites, exhibit significantly low phyllosilicate fractions, ranging from 1.9–4.2 % (Howard et al. 2010) and 0–3.3 % (Howard et al. 2014), respectively. One of the distinctive characteristics of phyllosilicates is their layered silicate sheet crystal structure, reflected in their name ("phyllo" means a leaf or something flat such as a leaf in Greek, Elmi 2023). Due to this crystal structure, microtextures (e.g., fibrous or flaky puff pastry-like (FPP) structures) are found in terrestrial phyllosilicate samples (Kumari & Mohan 2021). Not only in terrestrial samples but also in the hydrated meteorite samples, the phyllosilicates have FPP structures (Lee et al. 2014). Moreover, Noguchi et al. (2023) examined the regolith samples from the hydrated asteroid (162173) Ryugu. By using the field emission scanning electron microscope, Noguchi et al. (2023) found that the samples are covered by the dehydrated smooth layer, possibly modified by solar wind irradiation. When seeing the interior of samples protected from solar wind exposure, they found the phyllosilicates have FPP microtexture. Studies of meteorites (Lee et al. 2014) and regolith samples from Ryugu (Noguchi et al. 2023) suggest that asteroidal phyllosilicates have FPP microtextures similar to those in terrestrial samples. When the phyllosilicates experience space weathering, such as solar wind irradiation, they are dehydrated, and their submicrometer-size textures are modified. This phenomenon has also been observed in the experiments with meteorites (Zhang et al. 2022).

The submicrometer-sized structure in the phyllosilicates is comparable to or smaller than the wavelength of V- and R_C-bands. Thus, the microtexture in phyllosilicates could be one

of the possible surface features contributing to the deep NPBs observed in hydrated asteroids. Our suggestion is compatible with previous findings since the microtexture can exist regardless of other surface texture properties, such as the grain size distribution and the porosity. For example, the inherent microtexture of phyllosilicates could explain the deep NPBs observed in both CM-/CI-type meteoric samples and hydrated (CM- and CI-like) asteroids. Note that meteoric samples and asteroid surface regolith are likely to have different grain size distributions or porosity due to variations in sample preparation procedures or different environments (e.g., the surface gravity). In addition, the inherent microtexture of phyllosilicates can explain the weak correlation between NPBs and the diameters of the dark asteroids. The large asteroids (where fine particles may cover their surface due to their large gravity, MacLennan & Emery 2022) do not exhibit a deep P_{\min} . Fig. 6a shows the P_{\min} , h , and the size of the dark asteroids. We find that the largest asteroid (i.e., (1) Ceres, whose diameter is ~ 1000 km) has the intermediate P_{\min} while the asteroids with the deepest P_{\min} (i.e., (99) Dike) have the size of $\lesssim 100$ km. Our suggestion is also compatible with the previous near-infrared (NIR) polarimetric observations. The NIR polarimetric observation of the hydrated asteroid, (1) Ceres (Usui et al. 2019), has been done (Masiero et al. 2022; Bach et al. 2024b) with three different bands: J -, H -, and K_S -bands (the central wavelengths of $\lambda = 1.253, 1.632,$ and $2.146 \mu\text{m}$). In these three bands, P_{\min} and α_0 do not show the noticeable wavelength dependency. One of the interpretations suggested by Bach et al. (2024b) is the existence of submicrometer-sized particles on (1) Ceres, which is compatible with our consideration that the submicrometer-size structure may exist on the hydrated asteroids.

We further compare the thermal inertia (Γ) of dark asteroids with their polarimetric properties. Γ is another surface property influenced by the surface texture, including porosity and grain size parameters (Gundlach & Blum 2013; MacLennan & Emery 2022). In Fig. 6b, we compare the Γ of dark asteroids from MacLennan & Emery (2022) with $|P_{\min}|$. We exclude four asteroids, (87) Sylvania, (227) Philosphia, (283) Emma, and (444) Ggyptis, due to their large uncertainties of thermal inertia values, as they have Γ of $70 \pm 60, 125 \pm 90, 110 \pm 105,$ and $74 \pm 74 \text{ J m}^{-2} \text{K}^{-1} \text{s}^{-1/2}$, respectively. Additionally, two NEAs, (3200) Phaethon and (155140) 2005 UD, are excluded because their short heliocentric distance may affect the hydration status. In Fig. 6b, Γ values of asteroids fall within the range of $10\text{--}74 \text{ J m}^{-2} \text{K}^{-1} \text{s}^{-1/2}$, which is relatively small values compared to the overall range of Γ ($1\text{--}1000 \text{ J m}^{-2} \text{K}^{-1} \text{s}^{-1/2}$) reported in MacLennan & Emery (2022). Furthermore, we find that there is no noticeable correlation between P_{\min} and Γ . The lack of correlation may indicate that the submicrometer-size structure producing the deep NPBs (i.e., microtexture of phyllosilicates) may not strongly influence Γ , which requires further study.

4.2.3. Water ice

Dougherty & Geake (1994) reported that ice frost formed at low temperatures causes the deep NPB. However, it is unlikely that ice frost is the primary cause of the deep NPB observed in hydrated asteroids, given the shape of the NPB. Ice frost makes P_{\min} occur at small phase angles ($\alpha_{\min} \lesssim 5^\circ$). In contrast, hydrated asteroids that have been observed at $\alpha \lesssim 5^\circ$ exhibit α_{\min} at $\sim 10^\circ$, as shown in Fig. 3j, k, and l. Additionally, the polarimetric properties of hydrated asteroids do not show a correlation with the depth of the absorption feature near $3.1 \mu\text{m}$, indicative of surface ice (Usui et al. 2019).

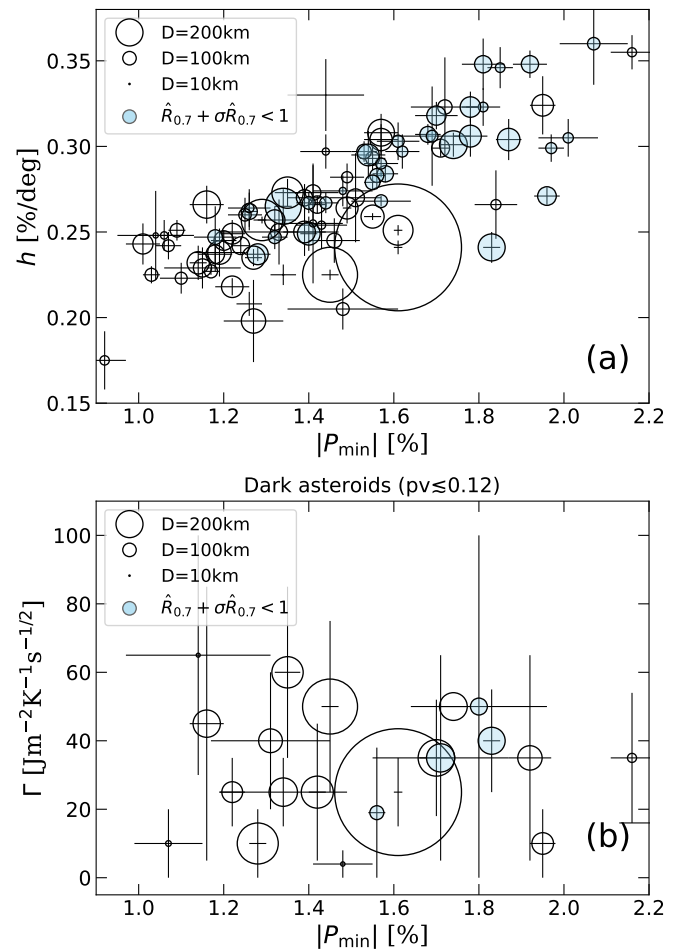


Fig. 6. (a) Comparison between the polarimetric properties (P_{\min} and h) with the diameters. (b) Comparison between the polarimetric properties (P_{\min} and h) and the thermal inertia given in MacLennan & Emery (2022). The Ch-type asteroids (DeMeo et al. 2009) are colored by the sky blue. In both (a) and (b), asteroids with $R_{0.7} + \sigma R_{0.7} < 1$ (i.e., Ch-type asteroids) are colored.

4.3. Possible physical mechanism enhanced the NPBs of hydrated asteroids

Several physical mechanisms have been proposed to explain NPBs (Lyot 1929; Öhman 1955; Hopfield 1966; Kolokolova 1990; Muinonen 1990; Shkuratov et al. 1994, 2002; Belskaya et al. 2005). Among them, the coherent back-scattering mechanism (CB, Hapke 1993) is the most significantly investigated (Mishchenko & Dlugach 1993; Shkuratov et al. 1994; Muinonen et al. 2002; Grynko et al. 2022). The CB is an interference mechanism that contributes not only to NPBs but also to the photometric opposition effect (Hapke 1990; Mishchenko & Dlugach 1993; Dlugach & Mishchenko 1999; Belskaya & Shevchenko 2000; Muinonen et al. 2002). Therefore, if the deep NPBs in hydrated asteroids result from CB, OE should also exhibit a correlation with NPBs and the spectral properties associated with hydrated minerals. To test this hypothesis, we compared the properties of PhotPC, including $\text{OE}_{0.3^\circ}$, polarimetric and spectroscopic features in Sect. 3.2.

In Sect. 3.2, $\text{OE}_{0.3^\circ}$ exhibits the correlations with various NPB parameters, particularly a strong correlation ($\rho > 0.8$) with P_{\min} . It is noteworthy that this $\text{OE}_{0.3^\circ}\text{--}P_{\min}$ relation shows the strongest correlation among all observation quantities in this

study. Such a strong correlation could suggest that there may be a common mechanism that governs both $OE_{0.3^\circ}$ and P_{\min} . Based on the previous studies that CB contributes to both NPBs and OE and the strong correlations between P_{\min} and $OE_{0.3^\circ}$ of dark asteroids, we think that CB is the responsible mechanism for strong NPBs and OE of hydrated asteroids. Notably, as well as dark asteroids, we also found a strong correlation ($\rho > 0.6$) between $OE_{0.3^\circ}$ (Belskaya & Shevchenko 2000) and NPB parameters (Lupishko 2018) in 15 bright asteroids ($p_V=0.13\text{--}0.55$, mainly S- and E-types asteroids), further supporting a common mechanism responsible for both OE and NPBs. Additionally, $OE_{0.3^\circ}$ shows moderately good correlations with \hat{R}_{UV} , $\hat{R}_{0.7}$, and $\hat{R}_{2.7}$, with $\rho > 0.4$. These findings imply that for dark asteroids exhibiting stronger hydration signatures, CB may become more pronounced on their surfaces, resulting in strong NPBs and OE. To understand how the surface properties of the hydrated asteroids enhance CB, we further discuss the surface properties that contribute to OE enhancement.

The OE has been observed in various airless bodies, including dark asteroids. Belskaya & Shevchenko (2000) compared $OE_{0.3^\circ}$ of multiple types of asteroids, including 10 dark ones. They notice a correlation between albedo and $OE_{0.3^\circ}$ within the dark asteroids ($p_V \lesssim 0.1$), where higher albedo values correspond to stronger OE. Afterward, Shevchenko & Belskaya (2010) expanded the dark asteroid sample size and found a similar correlation between albedo and $OE_{0.3^\circ}$ within the p_V range of 0.03 to 0.12, consistent with the findings in Belskaya & Shevchenko (2000). Additionally, Shevchenko et al. (2012) observed three very dark Trojan asteroids and found no evidence of OE from these asteroids. These results suggest that OE is enhanced as the albedo of the asteroids increases. These observational findings are aligned with Hapke (1993), who explained that CB becomes stronger when the albedo of objects increases.

However, the strength of OE of dark asteroids may not be explained by albedo alone. In Belskaya & Shevchenko (2000), $OE_{0.3^\circ}$ values scatter in the wide if limiting only low albedo asteroids ($p_V = 0.04\text{--}0.08$). In addition, among C-complex asteroids with similar albedo values, their $OE_{0.3^\circ}$ values show nearly a twofold difference (from about 0.1 to 0.2 mag). Shevchenko & Belskaya (2010) also noticed a weak correlation between albedo and the strength of OE for asteroids with $p_V = 0.04\text{--}0.08$. This evidence implies that there could be surface properties other than albedo that influence OE, as suggested by Belskaya & Shevchenko (2000). Our comparison with polarimetric, spectral properties, and p_V^* in Sect. 4.2.1 also indicates that albedo alone may not be the primary contributor to the deep NPBs of hydrated asteroids. Especially in Fig. 5h, despite the limited sample size, we could not find a significant correlation between $OE_{0.3^\circ}$ and p_V^* .

Another surface property, submicrometer-sized structure, is widely recognized as a contributor to CB. Laboratory and theoretical studies found that powder-like regolith layers show OE due to CB (Kuga & Ishimaru 1984; van der Mark et al. 1988). Later, Mishchenko & Dlugach (1992) examined the OE of Saturn's rings through a computational approach and demonstrated that submicrometer-sized particles reproduce the observational result well. They interpreted the OE of Saturn's rings as arising from a light scattering on the surface of individual particles (i.e., microtexture) rather than inter-particle light scattering. Subsequent research explored the relationship between submicrometer-sized particles and CB (Helfenstein et al. 1997; Dlugach & Mishchenko 2013). Furthermore, simulation work has shown that even a single particle with surface roughness can exhibit OE (Zubko et al. 2008). Jeong et al. (2020) inves-

tigated OE occurring on the Moon and proposed a correlation between CB and the amount of submicrometer-sized particles. These studies show that submicrometer particles (or microtexture) enhance the OE. In Sect. 3, we found that asteroids exhibiting strong hydration signatures show deep NPB and strong OE due to enhanced CB. This finding suggests that hydrated asteroids are covered with large amounts of submicrometer-sized structures, which might be microtextures in phyllosilicate, as we discussed in Sect. 4.2.2.

4.4. Potentiality of polarimetry for hydrated asteroids identification

As we demonstrated throughout this paper, polarimetry, especially the P_{\min} value, could be an indicator for the hydrated asteroid research since both CM- and CI-like asteroids have the deep P_{\min} . Asteroids with the $0.7\ \mu\text{m}$ band absorption accompanied with the $2.7\ \mu\text{m}$ feature (Vilas 1994). However, even if the absence of $0.7\ \mu\text{m}$ band, the $2.7\ \mu\text{m}$ band may still be present in the spectra (Fornasier et al. 2014). Thus, the absence of the $0.7\ \mu\text{m}$ absorption band does not necessarily indicate a lack of aqueous alteration on the asteroids (McAdam et al. 2016). In addition, the low-contrast $0.7\ \mu\text{m}$ band can obscure the absorption in spectra if a signal-to-noise ratio is low (Fornasier et al. 2014). Determination of $2.7\ \mu\text{m}$ band and UV drop-off is not easy. Telluric atmosphere makes ground-based observations of the $2.7\ \mu\text{m}$ bands impossible (Usui et al. 2019; Ivezić et al. 2022). Accurate determination of UV drop-off is challenging due to the significant decrease in the atmospheric transmittance in the wavelength due to the Rayleigh scattering. The selection of the comparison stars is also a difficult issue in the UV range (Tatsumi et al. 2022). As a result, most asteroid spectroscopic surveys from the ground do not cover the UV range and $2.7\ \mu\text{m}$ wavelength (Bus & Binzel 2002; Lazzaro et al. 2004; DeMeo et al. 2009). Consequently, among dark asteroids classified based on the $0.45\ \mu\text{m}$ to $2.4\ \mu\text{m}$ range, there could be hidden hydrated asteroids, like CI-like asteroids, not classified as Ch-type asteroids. Such a situation makes it difficult to understand the distribution of hydrated asteroids in the Solar System. However, P_{\min} can be derived relatively easily from the ground in the optical wavelength. The observation geometry of the main belt asteroids favors the determination of P_{\min} because they are usually located around $\alpha \sim 10^\circ$. In our polarimetric data, 48% (90 among 186) of dark asteroids with known P_{\min} values have the deep P_{\min} ($\lesssim -1.5\%$). This percentage value is larger than those of SMASSII, where 28% (154 out of 559²) of dark asteroids are classified as Ch-type asteroids (Bus & Binzel 2002).

Moreover, our findings introduce a new method for identifying CI-like asteroids. So far, both the $0.7\ \mu\text{m}$ and $2.7\ \mu\text{m}$ bands data are required to identify if the asteroids are CI-like or CM-like. As we stated, the combination of spectroscopy and polarimetry could allow us to discriminate CI-like and CM-like asteroids. Importantly, both $\hat{R}_{0.7}$ and P_{\min} can be obtained with a relatively low cost from ground-based observatories. We expect to increase the sample size of identified CI-like and CM-like asteroids via optical polarimetry and spectroscopy.

Lastly, SPHEREx (the Spectro-Photometer for the History of the Universe, Epoch of Reionization, and Ices Explorer; Doré et al. 2018; Korngut et al. 2018; Crill et al. 2020), a 2-year NASA MIDEX mission, will deliver an all-sky spectral cube. Through-

² These asteroids counts are obtained from the web-based Small-Body Database Query (https://ssd.jpl.nasa.gov/tools/sbdb_query.html) [Online Accessed, 2024 May 26].

out the mission, it is expected to increase the number of asteroids observed near $2.7\ \mu\text{m}$ by several orders of magnitude (Ivezic et al. 2022). At this point, polarimetry is expected to create a synergy effect with SPHEREx. As we compared with AKARI's spectra, the increase of the number by SPHEREx would unveil the nature of hydrated asteroids in combination with polarimetry. For example, simultaneous ground-based observations may be necessary to correct intrinsic rotational variability in SPHEREx asteroid spectra. At this point, P_{\min} could help prioritize ground-based observation targets among the asteroids scheduled to be observed by SPHEREx.

4.5. Summary

This study aims to understand the deep NPBs of Ch-type asteroids. We conducted polarimetric observations of 52 dark asteroids, including the 31 Ch-type asteroids, from 2020 March 23 to 2023 November 02 (a total of 50 nights). We compiled our polarimetric data with various observation measurements, including polarimetric, spectroscopic, and photometric archival data. In total, we analyzed polarimetric data of 199 dark asteroids. By comparing the observational properties, we found the following:

- (i) There are notable correlations between P_{\min} and the spectral properties (\hat{R}_{UV} , $\hat{R}_{0.7}$, and $\hat{R}_{2.7}$) associated with the hydrated minerals. Moreover, other NPB properties (h , α_0 , and α_{\min}) also show correlations with these three spectral properties. Most combinations exhibit moderately good linear correlations ($\rho > 0.4$), particularly $\hat{R}_{UV}-P_{\min}$, $\hat{R}_{UV}-\alpha_0$, and $\hat{R}_{0.7}-P_{\min}$, which exhibit strong correlations ($\rho > 0.6$).
- (ii) Most combinations between NPBs and photometric properties ($OE_{0.3^\circ}$ and b) exhibit moderate correlations ($\rho > 0.4$), with $OE_{0.3^\circ}-P_{\min}$ showing the strongest linear correlation ($\rho > 0.8$). Meanwhile, most spectral properties (\hat{R}_{UV} , $\hat{R}_{0.7}$, and $\hat{R}_{2.7}$) associated with hydrated minerals also show moderate good correlations with $OE_{0.3^\circ}$ and b .
- (iii) Deep $|P_{\min}|$ values in NPBs are likely to be observed not only in Ch-type asteroids associated with CM meteorites but also in some dark asteroids, categorized as non-Ch-type and linked with CI meteorites.
- (iv) Within dark asteroids (mainly C-complex), polarimetric properties show a weak correlation with the geometric albedo, thermal properties, and the asteroid's diameters. We propose that the submicrometer-sized structure of the regolith grain (i.e., FPP structure of phyllosilicates) may enhance CB on the asteroidal surface, contributing to the distinctive NPBs of hydrated asteroids.

Acknowledgements

This research at SNU was supported by a National Research Foundation of Korea (NRF) grant funded by the Korean government (MEST) (No. 2023R1A2C1006180). The Pirka telescope is operated by the Graduate School of Science, Hokkaido University, and is partially supported by the Optical & Near-Infrared Astronomy Inter-University Cooperation Program, MEXT, of Japan. S.H. was supported by the Hypervelocity Impact Facility (former name: the Space Plasma Laboratory), ISAS, JAXA. D.K. was supported by JSPS KAKENHI (No. JP23K03484). During the polarimetric observation period, J.G. and M.I. were supported by the staff members at Nayoro Observatory, Mr. Y. Murakami, Mr. F. Watanabe, and Ms. Y. Kato. We also appreciate the anonymous reviewer for their careful reading and insightful comments.

Data Availability

The observational data are available in Zenodo³ (link will be added). The source codes and scripts for the data analyses, plots, and resultant data tables are available via the GitHub service⁴. The analyzed polarimetric, spectroscopic, and photometric observational measurements in this study are also shared via GitHub (will be prepared as soon as possible).

References

- Arredondo, A., Campins, H., Pinilla-Alonso, N., et al. 2021, *Icarus*, 368, 114619
- Bach, Y. P., Ishiguro, M., Takahashi, J., et al. 2024a, *A&A*, 684, A80
- Bach, Y. P., Ishiguro, M., Takahashi, J., et al. 2024b, *A&A*, 684, A81
- Belskaya, I. N., Fornasier, S., Tozzi, G. P., et al. 2017, *Icarus*, 284, 30
- Belskaya, I. N., Lvasseur-Regourd, A.-C., Cellino, A., et al. 2009, *Icarus*, 199, 97
- Belskaya, I. N. & Shevchenko, V. G. 2000, *Icarus*, 147, 94
- Belskaya, I. N., Shkuratov, Y. G., Efimov, Y. S., et al. 2005, *Icarus*, 178, 213
- Bendjoya, P., Cellino, A., Rivet, J. P., et al. 2022, *A&A*, 665, A66
- Bowell, E., Hapke, B., Domingue, D., et al. 1989, in *Asteroids II*, ed. R. P. Binzel, T. Gehrels, & M. S. Matthews (Tucson: University of Arizona Press), 524–556
- Bus, S. J. & Binzel, R. P. 2002, *Icarus*, 158, 106
- Bus, S. J. B. 1999, PhD thesis, Massachusetts Institute of Technology
- Cellino, A., Bagnulo, S., Gil-Hutton, R., et al. 2015, *MNRAS*, 451, 3473
- Cellino, A., Yoshida, F., Anderlucci, E., et al. 2005, *Icarus*, 179, 297
- Chapman, C. R., Morrison, D., & Zellner, B. 1975, *Icarus*, 25, 104
- Clark, B. E., Bus, S. J., Rivkin, A. S., Shepard, M. K., & Shah, S. 2004, *AJ*, 128, 3070
- Clark, B. E., Ziffer, J., Nesvorný, D., et al. 2010, *J. Geophys. Res. (Planets)*, 115, E06005
- Crill, B. P., Werner, M., Akeson, R., et al. 2020, *Proc. SPIE*, 1144301
- de León, J., Pinilla-Alonso, N., Campins, H., Licandro, J., & Marzo, G. A. 2012, *Icarus*, 218, 196
- DeMeo, F. E., Binzel, R. P., Slivan, S. M., & Bus, S. J. 2009, *Icarus*, 202, 160
- DeMeo, F. E., Burt, B. J., Marsset, M., et al. 2022, *Icarus*, 380, 114971
- DeMeo, F. E. & Carry, B. 2013, *Icarus*, 226, 723
- Devogèle, M., Cellino, A., Bagnulo, S., et al. 2017, *MNRAS*, 465, 4335
- Dlugach, Z. M. & Mishchenko, M. I. 1999, *Sol. Syst. Res.*, 33, 472
- Dlugach, Z. M. & Mishchenko, M. I. 2013, *Sol. Syst. Res.*, 47, 454
- Dollfus, A. 1998, *Icarus*, 136, 69
- Dollfus, A. & Geake, J. E. 1977, *Philos. Trans. Roy. Soc. Lond. Ser.*, 285, 397
- Doré, O., Werner, M. W., Ashby, M. L. N., et al. 2018, arXiv e-prints, arXiv:1805.05489
- Dougherty, L. M. & Geake, J. E. 1994, *MNRAS*, 271, 343
- Elmi, C. 2023, *Encyclopedia*, 3, 1439
- Fornasier, S., Lantz, C., Barucci, M. A., & Lazzarin, M. 2014, *Icarus*, 233, 163
- Gaffey, M. J. & McCord, T. B. 1979, in *Asteroids*, ed. T. Gehrels & M. S. Matthews (University of Arizona Press), 688–723
- Gartelle, G. M., Hardersen, P. S., Izawa, M. R. M., & Nowinski, M. C. 2021, *Icarus*, 354, 114043
- Geake, J. E. & Dollfus, A. 1986, *MNRAS*, 218, 75
- Geake, J. E. & Geake, M. 1990, *MNRAS*, 245, 46
- Geake, J. E., Geake, M., & Zellner, B. H. 1984, *MNRAS*, 210, 89
- Geem, J., Ishiguro, M., Bach, Y. P., et al. 2022a, *A&A*, 658, A158
- Geem, J., Ishiguro, M., Granvik, M., et al. 2023, *MNRAS*, 525, L17
- Geem, J., Ishiguro, M., Takahashi, J., et al. 2022b, *MNRAS*, 516, L53
- Gil-Hutton, R. & Cañada-Assandri, M. 2012, *A&A*, 539, A115
- Gil-Hutton, R. & García-Migani, E. 2017, *A&A*, 607, A103
- Grynkó, Y., Shkuratov, Y., Alhaddad, S., & Foerstner, J. 2022, *Icarus*, 384, 115099
- Gundlach, B. & Blum, J. 2013, *Icarus*, 223, 479
- Hadamcik, E., Renard, J. B., Lasue, J., Lvasseur-Regourd, A. C., & Ishiguro, M. 2023, *MNRAS*, 520, 1963
- Hamilton, V. E., Simon, A. A., Christensen, P. R., et al. 2019, *Nat. Astron.*, 3, 332
- Hapke, B. 1990, *Icarus*, 88, 407
- Hapke, B. 1993, *Theory of reflectance and emittance spectroscopy* (Cambridge University Press)
- Hasegawa, S., Marsset, M., DeMeo, F. E., et al. 2024, *AJ*, 167, 224
- Helfenstein, P., Veverka, J., & Hillier, J. 1997, *Icarus*, 128, 2
- Hiroi, T., Pieters, C. M., Zolensky, M. E., & Lipschutz, M. E. 1993, *Science*, 261, 1016

³ <https://zenodo.XXXXXX>

⁴ https://github.com/Geemjy/Geem_AA_2024

- Hiroi, T., Zolensky, M. E., & Pieters, C. M. 2001, *Science*, 293, 2234
- Hopfield, J. J. 1966, *Science*, 151, 1380
- Howard, K., Benedix, G., Bland, P., & Cressey, G. 2010, *Geochim. Cosmochim. Acta*, 74, 5084
- Howard, K. T., Alexander, C. M. O., & Dyl, K. A. 2014, in 45th Annual Lunar and Planetary Science Conference, Lunar and Planetary Science Conference, 1830
- Howard, K. T., Benedix, G. K., Bland, P. A., & Cressey, G. 2009, *Geochim. Cosmochim. Acta*, 73, 4576
- Ishiguro, M., Bach, Y. P., Geem, J., et al. 2022, *MNRAS*, 509, 4128
- Ishiguro, M., Kuroda, D., Watanabe, M., et al. 2017, *AJ*, 154, 180
- Ito, T., Ishiguro, M., Arai, T., et al. 2018, *Nat. Commun.*, 9, 2486
- Ivezić, Ž., Ivezić, V., Moeyens, J., et al. 2022, *Icarus*, 371, 114696
- Jeong, M., Choi, Y.-J., Kim, S. S., & Shkuratov, Y. G. 2020, *J. Geophys. Res. (Planets)*, 125, e06164
- Jones, T. D., Lebofsky, L. A., Lewis, J. S., & Marley, M. S. 1990, *Icarus*, 88, 172
- Kawakami, A., Itoh, Y., Takahashi, J., Tozuka, M., & Takayama, M. 2022, *Stars and Galaxies*, 4, 5
- King, A. J., Schofield, P. F., Howard, K. T., & Russell, S. S. 2015, *Geochim. Cosmochim. Acta*, 165, 148
- Kokolova, L. O. 1990, *Icarus*, 84, 305
- Korngut, P. M., Bock, J. J., Akesson, R., et al. 2018, *Proc. SPIE*, 10698, 106981U
- Kuga, Y. & Ishimaru, A. 1984, *J. Opt. Soc. Am. A*, 1, 831
- Kumari, N. & Mohan, C. 2021, in *Clay and Clay Minerals*, ed. G. M. D. Nascimento
- Kuroda, D., Geem, J., Akitaya, H., et al. 2021, *ApJ*, 911, L24
- Kwon, Y. G., Bagnulo, S., & Cellino, A. 2023, *A&A*, 677, A146
- Kwon, Y. G., Hasegawa, S., Fornasier, S., Ishiguro, M., & Agarwal, J. 2022, *A&A*, 666, A173
- Lazzaro, D., Angeli, C. A., Carvano, J. M., et al. 2004, *Icarus*, 172, 179
- Lebofsky, L. A., Jones, T. D., Owensby, P. D., Feierberg, M. A., & Consolmagno, G. J. 1990, *Icarus*, 83, 16
- Lee, M. R., Lindgren, P., & Sofe, M. R. 2014, *Geochim. Cosmochim. Acta*, 144, 126
- López-Sisterna, C., García-Migani, E., & Gil-Hutton, R. 2019, *A&A*, 626, A42
- Lupishko, D. F. 2018, *Sol. Syst. Res.*, 52, 98
- Lupishko, D. F. 2019, NASA Planetary Data System, id. urn:nasa:pds:asteroid_polarimetric_database::1.0
- Lupishko, D. F. & Mohamed, R. 1996, *Icarus*, 119, 209
- Lyt, B. 1929, PhD thesis, Université Pierre et Marie Curie (Paris VI), France
- MacLennan, E. M. & Emery, J. P. 2022, *Planet. Sci. J.*, 3, 47
- Masiero, J. R., Tinyanont, S., & Millar-Blanchaer, M. A. 2022, *Planet. Sci. J.*, 3, 90
- McAdam, M., Sunshine, J. M., Kelley, M. S., & Bus, S. J. 2016, in *AAS/Division for Planetary Sciences Meeting Abstracts #48*, Vol. 48, 510.05
- McAdam, M. M. 2017, PhD thesis, University of Maryland, College Park
- Mishchenko, M. I. & Dlugach, J. M. 1993, *Planet. Space Sci.*, 41, 173
- Mishchenko, M. I. & Dlugach, Z. M. 1992, *MNRAS*, 254, 15P
- Muinenen, K., Penttilä, A., Cellino, A., et al. 2009, *Meteorit. Planet. Sci.*, 44, 1937
- Muinenen, K., Piironen, J., Shkuratov, Y. G., Ovcharenko, A., & Clark, B. E. 2002, in *Asteroids III*, ed. W. F. Bottke Jr., A. Cellino, P. Paolicchi, & R. P. Binzel, 123–138
- Muinenen, K., Uvarova, E., Martikainen, J., et al. 2022, *FrASS*, 9, 821125
- Muinenen, K. O. 1990, PhD thesis, University of Helsinki, Finland
- Neeley, J., Clark, B., Ockert-Bell, M., et al. 2014, *Icarus*, 238, 37
- Noguchi, T., Matsumoto, T., Miyake, A., et al. 2023, *Nat. Astron.*, 7, 170
- Öhman, Y. 1955, *Stockholm Obs. Ann.*, 18, 1
- Oriol, A.-P., Virgile, A., Colin, C., et al. 2023, *PeerJ Computer Science*, 9, e15116
- Rayner, J. T., Toomey, D. W., Onaka, P. M., et al. 2003, *PASP*, 115, 362
- Reddy, V. & Sanchez, J. A. 2016, NASA Planetary Data System, id. EAR-A-10046-3-REDDYMBSPEC-V1.0
- Rivkin, A. S., Howell, E. S., Lebofsky, L. A., Clark, B. E., & Britt, D. T. 2000, *Icarus*, 145, 351
- Rivkin, A. S., Howell, E. S., Vilas, F., & Lebofsky, L. A. 2002, in *Asteroids III*, ed. W. F. Bottke Jr., A. Cellino, P. Paolicchi, & R. P. Binzel, 235–253
- Shevchenko, V. G. & Belskaya, I. N. 2010, in *European Planetary Science Congress*, 738
- Shevchenko, V. G., Belskaya, I. N., Krugly, Y. N., Chiomy, V. G., & Gaftonyuk, N. M. 2002, *Icarus*, 155, 365
- Shevchenko, V. G., Belskaya, I. N., Slyusarev, I. G., et al. 2012, *Icarus*, 217, 202
- Shevchenko, V. G., Chiorny, V. G., Gaftonyuk, N. M., et al. 2008, *Icarus*, 196, 601
- Shevchenko, V. G. & Tedesco, E. F. 2006, *Icarus*, 184, 211
- Shkuratov, Y. G., Bondarenko, S., Ovcharenko, A., et al. 2006, *J. Quant. Spectr. Rad. Transf.*, 100, 340
- Shkuratov, Y. G., Muinenen, K., Bowell, E., et al. 1994, *Earth, Moon, Planets*, 65, 201
- Shkuratov, Y. G., Ovcharenko, A., Zubko, E., et al. 2002, *Icarus*, 159, 396
- Spadaccia, S., Patty, C. H. L., Capelo, H. L., Thomas, N., & Pommerol, A. 2022, *A&A*, 665, A49
- Takir, D. & Emery, J. P. 2012, *Icarus*, 219, 641
- Takir, D., Emery, J. P., & McSween, H. Y. 2015, *Icarus*, 257, 185
- Takir, D., Emery, J. P., McSween, H. Y., et al. 2013, *Meteorit. Planet. Sci.*, 48, 1618
- Tatsumi, E., Tinaut-Ruano, F., de León, J., Popescu, M., & Licandro, J. 2022, *A&A*, 664, A107
- Tatsumi, E., Vilas, F., de León, J., et al. 2023, *A&A*, 672, A189
- Tedesco, E. F. 1994, in *Asteroids, Comets, Meteors 1993*, ed. A. Milani, M. di Martino, & A. Cellino, Vol. 160, 55–74
- Tholen, D. J. 1984, PhD thesis, University of Arizona
- Uehara, M., Nagashima, C., Sugitani, K., et al. 2004, *Proc. SPIE*, 5492, 661
- Umw, v. N. 1905, *Physikalische Zeitschrift*, 6, 674
- Usui, F., Hasegawa, S., Ootsubo, T., & Onaka, T. 2019, *PASJ*, 71, 1
- van der Mark, M. B., van Albada, M. P., & Legendijk, A. 1988, *Phys. Rev. B*, 37, 3575
- Vernazza, P., Marsset, M., Beck, P., et al. 2016, *AJ*, 152, 54
- Vilas, F. 1994, *Icarus*, 111, 456
- Vilas, F. & Gaffey, M. J. 1989, *Science*, 246, 790
- Watanabe, M., Takahashi, Y., Sato, M., et al. 2012, *Proc. SPIE*, 8446, 84462O
- Widorn, T. 1967, *Annalen der Universitaets-Sternwarte Wien, Dritter Folge*, 27, 109
- Zellner, B., Leake, M., Lebertre, T., Duseaux, M., & Dollfus, A. 1977, *Lunar Planet. Sci. Conf. Proc.*, 1, 1091
- Zellner, B., Tholen, D., & Tedesco, E. 2020, NASA Planetary Data System, id. urn:nasa:pds:gbo.ast.ecas.phot::1.0
- Zellner, B., Tholen, D. J., & Tedesco, E. F. 1985, *Icarus*, 61, 355
- Zhang, P., Tai, K., Li, Y., et al. 2022, *A&A*, 659, A78
- Ziffer, J., Campins, H., Licandro, J., et al. 2011, *Icarus*, 213, 538
- Zubko, E., Shkuratov, Y., Mishchenko, M., & Videen, G. 2008, *J. Quant. Spectr. Rad. Transf.*, 109, 2195

Appendix A: Updated Pirka/MSI polarimetric data analysis procedures

As we described in Sec. 2.1, we noticed that the WBS in the filter wheel is not firmly fixed and rotates randomly during slewing the telescope and rotating filter wheels for the data taken after 2021 March 2. This rotation causes the relative positions of o- and e-rays to change for every image. As illustrated in Fig. A1, we derive the tilted angle between o- and e-ray (θ_{TILT}) via the equation given by

$$\theta_{\text{TILT}} = \arctan((x_e - x_o)/(y_e - y_o)), \quad (\text{A.1})$$

where (x_o, y_o) and (x_e, y_e) are the xy coordinates of the target center in o- and e-rays. θ_{TILT} ranges from 0° to 360° . The rotation of the WBS results in a similar effect to the rotation of the instrument. Therefore, the WBS rotation affects the instrumental polarization (q_{inst} and u_{inst}) and the position angle offset of the instrument (θ_{off}), which are the calibration parameters that are dependent on the instrument rotator angle. We conducted observations of the unpolarized (UNPOL) and strongly polarized (SPOL) standard stars across a wide range of θ_{TILT} . As a result, we confirmed empirical correlations between θ_{TILT} and the calibration parameters (i.e., q_{inst} , u_{inst} , and θ_{off}). Based on the correlation, we updated the data reduction process by using the following equations:

$$\begin{pmatrix} q'_{\text{pol}} \\ u'_{\text{pol}} \end{pmatrix} = p_{\text{eff}} \begin{pmatrix} q_{\text{pol}} \\ u_{\text{pol}} \end{pmatrix}, \quad (\text{A.2})$$

where q_{pol} and u_{pol} are the stokes parameters of the targets and p_{eff} is the polarization efficiency of MSI. We confirmed that p_{eff} does not depend on the WBS rotation by taking pinhole images through a wire-grid filter. Next, the instrumental polarization of MSI can be corrected with the following equations:

$$\begin{pmatrix} q''_{\text{pol}} \\ u''_{\text{pol}} \end{pmatrix} = \begin{pmatrix} q'_{\text{pol}} \\ u'_{\text{pol}} \end{pmatrix} - \begin{pmatrix} \cos 2\theta'_{\text{rot1}} & -\sin 2\theta'_{\text{rot1}} \\ \sin 2\theta'_{\text{rot2}} & \cos 2\theta'_{\text{rot2}} \end{pmatrix} \begin{pmatrix} q_{\text{inst}} \\ u_{\text{inst}} \end{pmatrix}, \quad (\text{A.3})$$

where θ'_{rot1} and θ'_{rot2} are given by:

$$\theta'_{\text{rot1}} = \theta_{\text{rot1}} - \bar{\theta}_{\text{TILT}}, \quad \theta'_{\text{rot2}} = \theta_{\text{rot2}} - \bar{\theta}_{\text{TILT}}. \quad (\text{A.4})$$

Here, θ_{rot1} means the average instrument rotator angle during the exposure with HWP= 0° and 45° , while θ_{rot2} means the average angle with HWP= 22.5° and 67.5° . $\bar{\theta}_{\text{TILT}}$ is the average value of θ_{TILT} during the exposure with HWP= 0° , 45° , 22.5° , and 67.5° . We noted that θ_{TILT} remained nearly constant throughout the exposures when we tracked a target without slewing the telescope or rotating filter wheels. Then, the instrument position angle offset (θ'_{off}) can be derived via the equations given by:

$$\begin{pmatrix} q'''_{\text{pol}} \\ u'''_{\text{pol}} \end{pmatrix} = \begin{pmatrix} \cos 2\theta'_{\text{off}} & \sin 2\theta'_{\text{off}} \\ -\sin 2\theta'_{\text{off}} & \cos 2\theta'_{\text{off}} \end{pmatrix} \begin{pmatrix} q''_{\text{pol}} \\ u''_{\text{pol}} \end{pmatrix}, \quad (\text{A.5})$$

and

$$\theta'_{\text{off}} = \theta_{\text{off}} - \theta_{\text{ref}} + \bar{\theta}_{\text{TILT}}, \quad (\text{A.6})$$

where θ_{ref} denotes the position angle of the instrument relative to the telescope and is usually a fixed ($\theta_{\text{ref}} = -0.52^\circ$) for most observations, except for specialized observations such as UNPOL standard stars observations. Eqs. (A.3)–(A.6) are the modified versions of Eqs. (23)–(25) in Ishiguro et al. (2017).

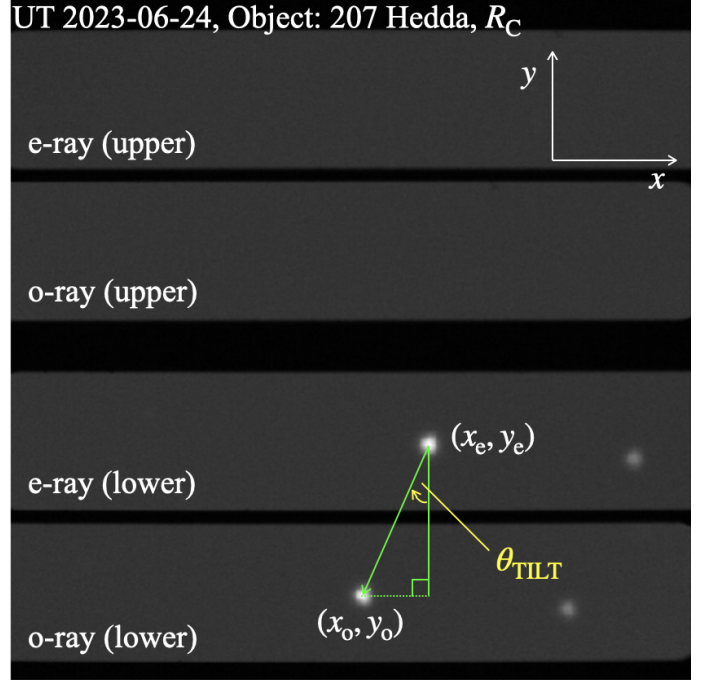


Fig. A1. Example R_C -band image of the asteroid, 207 Hedda, taken on UT 2023-06-24 in the polarization mode of the MSI. The xy coordinates of the target center in o- and e-rays are shown as (x_o, y_o) and (x_e, y_e) , respectively. θ_{TILT} is the tilted angle between the o- and e-rays components measured clockwise.

Appendix B: Wavelength dependency of P_r

To examine the wavelength dependency in P_r of dark asteroids in V- and R_C -bands, we compared the P_r values in these two bands. Hereafter, we refer them to as $P_{r,V}$ and P_{r,R_C} . For the comparison, we used polarization degree databases of 26 asteroids with a small uncertainty (i.e., $\sigma P_r < 0.1\%$). The asteroids used for the examination are (1) Ceres, (2) Pallas, (10) Hygiea, (13) Egeria, (19) Fortuna, (31) Euphrosyne, (41) Daphne, (48) Doris, (51) Nemausa, (56) Melete, (59) Elpis, (72) Feronia, (76) Freia, (708) Raphaela, (85) Io, (91) Aegina, (93) Minerva, (102) Miriam, (128) Nemesis, (200) Dynamene, (213) Lilaea, (238) Hypatia, (324) Bambergia, (335) Roberta, (350) Ornamenta, (372) Palma, (386) Siegena, (709) Fringilla, (409) Aspasia, (431) Nephele, (444) Gyptis, (451) Patientia, (679) Pax, and (704) Interamnia. These asteroids cover a wide range of taxonomy types of dark asteroids, including B-, F-, P-, G-, T-types, and C-complex asteroids in Tholen, SMASSII, or Bus-DeMeo taxonomy classifications (Tholen 1984; DeMeo et al. 2009).

In Fig. B2, we compared $P_{r,V}$ with P_{r,R_C} . Each data point represents a polarization degree obtained in both V- and R_C -bands at the same phase angle. Here, the same phase angle means the condition where the phase angle difference was less than 0.5° . We calculated the standard deviation of $(P_{r,R_C} - P_{r,V})$ and obtained $1\sigma = 0.108\%$, which is compatible with the result from Belskaya et al. (2009), who noted a 0.1% P_r change across these bands. The 1σ value is almost equivalent to the errors of our measurements in this study (see σP in Tables D1). Therefore, we concluded that there is no significant change in P_r between these two bands and used both V- and R_C -bands to fit the PPC. This conclusion is consistent with those of Masiero et al. (2022), where the authors suggested that the C-complex objects do not indicate a significant wavelength dependency in NPBs from B-band to H-band.

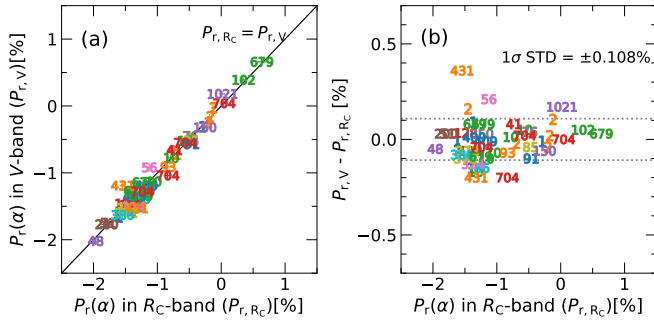


Fig. B2. Comparison in the P_r in V- and R_C -bands. (a) Each data point indicates the observed P_r of dark asteroids taken at the same phase angle in V- and R_C bands ($P_{r,V}$ and P_{r,R_C} , respectively). The marker indicates the asteroids' ID. The black solid line of $P_{r,V} = P_{r,R_C}$. (b) The difference between $P_{r,V}$ and P_{r,R_C} depending on P_{r,R_C} is shown. The dashed lines indicate the standard deviation of $P_{r,V} - P_{r,R_C}$, which is $\pm 0.108\%$.

Appendix C: Polarimetric observation circumstance

The observation circumstances are summarized in Tables C1.

Table C1. Observation circumstances

Target	Date (YY-MM-DD)	UT	Filter	N ^a	Exp ^b (s)	AM ^c	α^d (deg)	ϕ^e (deg)	r^f (au)	Δ^g (au)	Inst ^h
19 Fortuna	20-08-22	16:50–17:00	R _C	24	20	1.5–1.5	10.58	241.77	2.17	1.20	MSI
24 Themis	23-09-25	17:22–17:38	R _C	28	30	1.1–1.1	16.76	260.07	3.14	2.57	MSI
24 Themis	23-09-28	17:31–17:36	R _C	8	60	1.1–1.1	16.34	260.09	3.13	2.53	MSI
41 Daphne	22-08-17	11:35–11:48	R _C	28	15	1.6–1.6	25.25	103.57	2.23	1.66	MSI
49 Pales	20-08-22	16:33–16:43	R _C	24	20	1.3–1.3	10.95	238.46	2.58	1.65	MSI
54 Alexandra	23-08-22	10:58–11:05	R _C	24	10	2.8–2.8	15.91	78.13	2.18	1.28	MSI
54 Alexandra	23-08-24	11:10–11:27	R _C	24	40	2.6–2.7	16.68	78.67	2.18	1.30	MSI
54 Alexandra	23-09-24	12:31–12:38	R _C	12	40	3.2–3.4	24.69	80.67	2.20	1.60	MSI
54 Alexandra	23-09-28	10:38–10:52	R _C	24	30	2.3–2.4	25.20	80.41	2.20	1.64	MSI
58 Concordia	20-03-26	15:15–15:39	R _C	24	60	1.7–1.8	11.64	279.69	2.59	1.68	MSI
58 Concordia	20-05-07	15:30–15:54	R _C	24	60	1.8–2.0	7.49	129.53	2.59	1.62	MSI
58 Concordia	20-05-15	15:22–15:41	R _C	20	60	2.0–2.1	10.65	123.19	2.59	1.66	MSI
58 Concordia	22-11-28	09:15–12:33	R _C	48	60	1.2–2.9	5.08	45.07	2.79	1.82	WFGS2
66 Maja	20-03-23	12:17–12:40	R _C	24	0	1.2–1.2	9.43	115.10	2.76	1.84	MSI
66 Maja	20-03-26	14:05–16:34	R _C	56	60	1.3–1.9	10.57	114.44	2.77	1.86	MSI
66 Maja	20-03-29	16:41–17:20	R _C	36	60	2.2–2.9	11.64	113.92	2.77	1.89	MSI
66 Maja	20-04-12	15:16–15:40	R _C	24	60	1.9–2.2	15.70	112.48	2.79	2.03	MSI
66 Maja	22-11-06	11:17–12:04	R _C	44	60	2.3–2.8	24.16	70.01	2.37	1.96	MSI
70 Panopaea	23-08-23	18:07–18:21	R _C	24	30	1.3–1.3	22.76	259.66	2.60	2.49	MSI
91 Aegina	23-06-21	13:26–13:48	R _C	24	60	2.8–3.0	8.88	95.17	2.86	1.91	MSI
95 Arethusia	22-11-28	10:56–11:41	R _C	12	60	2.0–2.7	19.84	68.84	2.77	2.91	WFGS2
95 Arethusia	23-08-23	17:47–18:01	R _C	16	60	1.2–1.3	22.75	260.36	2.60	2.51	MSI
99 Dike	20-03-30	17:01–17:25	R _C	24	60	1.4–1.6	8.86	160.34	2.31	1.35	MSI
99 Dike	20-04-12	14:08–16:24	R _C	60	60	1.2–1.6	13.55	136.68	2.29	1.38	MSI
99 Dike	22-11-28	10:07–10:35	R _C	24	60	1.4–1.6	4.04	100.17	3.19	2.22	WFGS2
105 Artemis	22-11-28	15:17–15:17	R _C	4	60	1.5–1.5	11.32	36.11	2.78	1.90	WFGS2
111 Ate	23-06-21	11:45–12:04	R _C	20	60	2.9–3.5	23.13	113.67	2.49	2.56	MSI
111 Ate	23-06-26	11:05–11:26	R _C	28	40	2.5–2.9	22.70	114.08	2.50	2.63	MSI
128 Nemesis	22-08-07	16:22–16:28	R _C	16	5	1.8–1.8	17.40	255.36	2.45	1.64	MSI
142 Polana	23-06-25	16:10–16:35	R _C	24	60	2.1–2.3	23.27	246.99	2.42	1.87	MSI
144 Vibilia	23-06-24	17:00–17:09	R _C	12	60	3.7–4.1	27.00	247.22	2.04	2.24	MSI
144 Vibilla	23-08-30	18:22–18:44	R _C	28	20	1.2–1.2	28.93	257.31	2.04	1.57	MSI
144 Vibilla	23-09-01	19:16–19:29	R _C	28	20	1.1–1.1	28.71	257.62	2.04	1.56	MSI
147 Protogeneia	20-08-13	16:12–16:22	R _C	16	40	1.4–1.4	10.17	242.40	3.06	2.16	MSI
147 Protogeneia	20-08-21	15:14–15:25	R _C	24	20	1.4–1.4	7.57	240.36	3.06	2.11	MSI
147 Protogeneia	20-08-23	15:57–16:21	R _C	24	60	1.4–1.4	6.87	239.58	3.06	2.10	MSI
162 Laurentia	20-08-02	18:31–18:44	R _C	24	30	1.4–1.4	14.79	249.61	3.49	2.88	MSI
162 Laurentia	20-08-17	16:18–16:46	R _C	32	40	1.4–1.5	3.35	224.49	2.66	1.65	MSI
162 Laurentia	20-08-21	17:06–17:29	R _C	24	60	1.4–1.4	11.32	252.17	3.47	2.66	MSI
162 Laurentia	20-08-23	15:21–15:50	R _C	28	60	1.5–1.6	10.87	252.54	3.47	2.64	MSI
162 Laurentia	20-08-25	15:37–15:53	R _C	28	30	1.5–1.5	10.38	252.96	3.47	2.62	MSI
162 Laurentia	20-10-13	12:42–13:06	R _C	20	60	1.5–1.5	5.45	54.74	3.42	2.46	MSI
173 Ino	23-09-01	18:58–19:02	R _C	12	20	1.4–1.4	26.99	262.26	2.22	2.06	MSI
176 Iduna	23-06-25	14:09–14:23	R _C	24	30	1.4–1.4	10.05	137.70	3.50	2.63	MSI
176 Iduna	23-07-01	14:20–14:58	R _C	36	60	1.5–1.7	11.19	130.93	3.49	2.67	MSI
207 Hedda	23-06-20	14:18–14:37	R _C	24	40	3.4–3.7	9.52	86.44	2.23	1.25	MSI
207 Hedda	23-06-24	14:15–14:39	R _C	24	60	3.6–4.1	11.41	89.26	2.23	1.27	MSI
207 Hedda	23-06-26	14:24–14:38	R _C	16	60	3.9–4.3	12.32	90.37	2.23	1.28	MSI
209 Dido	23-06-26	14:47–15:01	R _C	16	40	4.3–4.6	8.18	279.99	3.01	2.06	MSI
233 Asterope	23-06-19	16:02–16:13	R _C	12	60	2.5–2.7	25.03	246.64	2.40	2.21	MSI
238 Hypatia	20-05-12	11:25–11:35	V	12	60	2.6–2.9	17.68	103.97	2.91	3.26	MSI
238 Hypatia	23-06-21	15:30–16:26	R _C	28	90	2.3–3.5	21.71	246.41	2.75	2.54	MSI
238 Hypetia	23-09-02	16:35–16:41	R _C	12	30	1.3–1.4	8.14	237.89	2.70	1.74	MSI
240 Vanadis	23-08-21	10:45–11:09	R _C	24	60	2.9–3.3	7.35	71.54	2.65	1.67	MSI
257 Silesia	20-08-13	15:49–16:01	R _C	16	40	1.6–1.6	10.39	252.83	3.03	2.13	MSI
257 Silesia	20-08-21	15:37–15:54	R _C	24	40	1.6–1.6	7.81	255.68	3.03	2.07	MSI
257 Silesia	20-08-23	17:26–17:40	R _C	24	30	1.7–1.8	7.10	256.78	3.02	2.06	MSI

continued from previous page

Target	Date (YY-MM-DD)	UT	Filter	N ^a	Exp ^b (s)	AM ^c	α^d (deg)	ϕ^e (deg)	r^f (au)	Δ^g (au)	Inst ^h
266 Aline	23-06-20	13:01–13:27	R _C	24	60	2.3–2.5	13.00	107.67	3.16	2.36	MSI
266 Aline	23-06-21	14:06–14:46	R _C	(24,4)	(90,60)	3.0–4.1	13.26	107.73	3.16	2.37	MSI
266 Aline	23-06-24	12:38–13:02	R _C	24	60	2.2–2.4	13.96	107.86	3.16	2.40	MSI
266 Aline	23-06-25	14:30–14:53	R _C	24	60	4.0–5.2	14.20	107.89	3.16	2.41	MSI
266 Aline	23-06-26	12:44–14:15	R _C	72	60	2.3–3.7	14.41	107.92	3.16	2.42	MSI
266 Aline	23-07-01	12:35–13:28	R _C	48	60	2.4–3.0	15.42	108.02	3.16	2.47	MSI
282 Clorinde	23-08-21	14:30–15:42	R _C	20	60	1.6–1.8	8.13	257.80	2.36	1.39	MSI
284 Amalia	23-06-21	12:49–13:19	R _C	28	60	2.2–2.5	25.49	110.64	1.98	1.24	MSI
308 Polyxo	20-07-31	16:17–16:26	R _C	16	30	1.6–1.6	10.27	241.05	2.65	1.71	MSI
308 Polyxo	20-08-08	18:18–18:42	R _C	20	40	2.1–2.3	7.06	237.38	2.66	1.68	MSI
308 Polyxo	20-08-09	18:30–18:30	R _C	4	40	2.3–2.3	6.65	236.66	2.66	1.67	MSI
308 Polyxo	20-08-17	16:52–17:06	R _C	24	30	1.8–1.9	3.34	224.43	2.66	1.65	MSI
308 Polyxo	20-08-21	18:18–18:26	R _C	24	15	3.1–3.3	1.83	200.79	2.66	1.65	MSI
308 Polyxo	20-10-13	11:56–12:21	R _C	24	60	1.9–2.0	17.85	71.88	2.67	1.98	MSI
357 Ninina	23-06-20	13:37–14:05	R _C	24	60	1.5–1.5	8.21	139.03	3.33	2.40	MSI
357 Ninina	23-07-01	13:36–14:13	R _C	36	60	1.6–1.7	10.65	124.85	3.32	2.46	MSI
368 Haidea	23-06-22	16:20–17:30	R _C	28	60	1.6–2.2	24.32	246.49	2.47	2.27	MSI
375 Ursula	20-08-02	18:12–18:22	R _C	16	30	1.4–1.4	15.03	244.57	2.82	2.02	MSI
375 Ursula	20-08-09	18:10–18:22	R _C	16	40	1.4–1.5	13.04	243.18	2.83	1.96	MSI
375 Ursula	20-08-16	15:17–17:37	R _C	16	20	1.4–1.4	10.80	241.00	2.83	1.92	MSI
375 Ursula	20-08-21	16:45–16:55	R _C	24	20	1.4–1.4	9.06	238.57	2.83	1.89	MSI
398 Admete	20-07-30	17:26–17:50	R _C	16	90	1.5–1.6	9.61	229.53	2.87	1.94	MSI
398 Admete	20-08-21	16:02–17:53	R _C	36	40	1.6–2.4	4.05	164.10	2.82	1.82	MSI
398 Admete	20-08-24	14:40–15:04	R _C	20	60	1.4–1.5	4.18	146.89	2.82	1.82	MSI
405 Thia	20-07-30	16:31–17:11	R _C	28	90	1.2–1.2	15.11	231.53	2.95	2.18	MSI
405 Thia	20-08-09	14:44–16:24	R _C	24	90	1.2–1.3	12.59	224.59	2.96	2.11	MSI
405 Thia	20-08-13	15:32–15:43	R _C	16	40	1.2–1.2	11.49	220.83	2.97	2.09	MSI
405 Thia	20-08-21	18:00–18:13	R _C	24	30	1.4–1.5	9.23	210.34	2.99	2.06	MSI
405 Thia	20-08-25	15:59–16:29	R _C	48	30	1.2–1.2	8.18	203.21	2.99	2.05	MSI
405 Thia	23-06-20	12:29–12:51	R _C	20	60	4.4–6.0	31.23	113.52	1.96	1.65	MSI
410 Chloris	23-06-21	12:24–12:42	R _C	16	60	1.8–2.0	25.81	113.65	2.33	2.12	MSI
442 Eichsfeldia	23-11-02	15:14–15:54	R _C	36	60	1.2–1.2	8.46	283.39	2.51	1.56	MSI
490 Veritas	20-07-31	14:52–15:06	R _C	12	90	2.2–2.4	9.79	107.14	3.12	2.20	MSI
490 Veritas	20-08-22	12:36–12:50	R _C	16	60	2.0–2.1	15.09	95.41	3.10	2.38	MSI
490 Veritas	22-11-28	13:18–14:17	R _C	48	60	1.7–2.5	12.97	290.32	3.12	2.35	WFGS2
503 Evelyn	20-04-11	14:36–14:59	R _C	24	60	1.7–1.9	22.69	111.27	2.36	1.76	MSI
503 Evelyn	20-04-13	14:05–14:29	R _C	24	60	1.5–1.7	22.98	111.06	2.37	1.79	MSI
503 Evelyn	20-05-07	13:36–14:30	R _C	48	60	2.0–2.8	24.76	109.85	2.40	2.10	MSI
503 Evelyn	20-05-15	13:33–14:44	R _C	52	90	2.2–4.2	24.75	109.78	2.41	2.21	MSI
586 Thekla	20-07-31	16:36–17:04	R _C	12	60	1.4–1.4	14.00	244.92	3.18	2.42	MSI
586 Thekla	20-08-12	16:00–16:36	R _C	16	60	1.4–1.4	11.04	243.94	3.17	2.30	MSI
586 Thekla	20-08-17	15:10–16:01	R _C	40	60	1.4–1.5	9.60	243.34	3.17	2.26	MSI
586 Thekla	20-08-21	16:21–16:34	R _C	24	30	1.4–1.4	8.35	242.67	3.17	2.23	MSI
586 Thekla	20-08-26	12:34–13:40	R _C	32	60	1.6–2.1	6.75	241.53	3.17	2.20	MSI
602 Marianna	20-03-24	15:39–16:03	R _C	24	60	1.7–1.9	9.66	107.35	3.57	2.73	MSI
602 Marianna	20-03-29	14:02–14:26	R _C	24	60	1.4–1.5	10.84	107.47	3.58	2.78	MSI
602 Marianna	20-04-11	15:39–16:03	R _C	20	60	2.7–3.4	13.36	107.85	3.60	2.95	MSI
602 Marianna	20-04-13	14:58–15:21	R _C	24	60	2.2–2.5	13.67	107.92	3.61	2.98	MSI
602 Marianna	23-06-19	16:22–16:32	R _C	12	60	2.8–3.0	24.57	246.58	2.44	2.22	MSI
618 Elfriede	23-06-26	12:29–12:29	R _C	4	60	1.9–1.9	5.29	249.01	9.79	9.28	MSI
771 Libera	20-08-22	15:58–16:25	R _C	24	60	2.4–2.9	11.31	110.64	3.04	2.16	MSI
776 Berbericia	20-03-23	12:56–13:20	R _C	24	60	1.1–1.1	8.03	181.28	3.32	2.40	MSI
776 Berbericia	20-03-26	12:58–13:22	R _C	24	60	1.1–1.1	8.41	174.30	3.32	2.41	MSI
776 Berbericia	20-03-29	15:28–16:12	R _C	36	60	1.1–1.2	8.89	167.78	3.32	2.43	MSI
776 Berbericia	20-04-12	12:28–13:06	R _C	36	60	1.1–1.1	11.45	146.60	3.33	2.52	MSI
776 Berbericia	20-05-07	14:51–15:15	R _C	24	60	1.5–1.6	15.55	126.98	3.35	2.77	MSI
776 Berbericia	20-05-15	16:02–16:26	R _C	24	60	2.5–3.0	16.41	123.16	3.36	2.87	MSI
776 Berbericia	23-09-02	16:49–16:55	R _C	12	30	2.1–2.2	22.82	266.39	2.51	2.58	MSI
821 Fanny	23-06-24	13:44–14:07	R _C	24	60	2.2–2.4	11.63	240.94	2.30	1.35	MSI
821 Fanny	23-06-26	15:21–15:50	R _C	28	60	1.8–1.8	10.75	239.03	2.31	1.34	MSI

continued from previous page

Target	Date (YY-MM-DD)	UT	Filter	N ^a	Exp ^b (s)	AM ^c	α^d (deg)	ϕ^e (deg)	r^f (au)	Δ^g (au)	Inst ^h
1015 Christa	23-06-25	12:39–13:02	R_C	24	60	1.7–1.8	10.76	115.96	3.47	2.63	MSI
1201 Strenua	23-06-25	13:11–14:03	R_C	48	60	1.9–2.1	11.72	113.71	2.74	1.84	MSI
1542 Schalen	23-09-24	12:45–13:09	R_C	24	60	1.5–1.7	9.68	247.13	2.73	1.80	MSI
1754 Cunningham	23-06-19	15:25–15:40	R_C	12	90	1.8–1.9	7.48	139.59	3.30	2.35	MSI
1754 Cunningham	23-06-24	13:10–13:33	R_C	24	60	1.5–1.6	8.60	131.83	3.29	2.37	MSI
1795 Woltjer	20-08-22	15:22–15:27	R_C	8	60	2.2–2.2	10.57	99.19	2.36	1.41	MSI
1867 Deiphobus	23-09-24	16:21–17:12	R_C	48	60	1.9–2.6	6.82	114.95	5.01	4.17	MSI
2569 Madeline	23-09-24	14:27–14:46	R_C	20	60	2.0–2.1	8.85	326.33	2.23	1.26	MSI

Notes. ^(a) Number of valid exposures, ^(b) Exposure time in seconds, ^(c) Airmass, ^(d) Median solar phase angle in degrees, ^(e) Position angle of the scattering plane in degrees, ^(f) Median heliocentric distance in au, ^(g) Median geocentric distance in au, ^(h) Instrument. The web-based JPL Horizon system (<http://ssd.jpl.nasa.gov/?horizons>) was used to obtain r , Δ , α , and ϕ .

Appendix D: Polarimetric result

The nightly averaged linear polarimetric results of asteroids observed in this study are summarized in Tables [D1](#).

Table D1. Observation circumstances

Target	Date (YY-MM-DD)	UT	Filter	α^a (deg)	P^b (%)	σP^c (%)	θ^d (deg)	$\sigma\theta^e$ (deg)	P_r^f (%)	θ_r^g (deg)	Inst ^h
19 Fortuna	20-08-22	16:50–17:00	R_C	10.58	1.78	0.03	63.35	0.53	-1.78	91.58	MSI
24 Themis	23-09-25	17:22–17:38	R_C	16.76	0.93	0.05	88.62	1.49	-0.89	98.55	MSI
24 Themis	23-09-28	17:31–17:36	R_C	16.34	1.32	0.14	87.42	3.13	-1.27	97.33	MSI
41 Daphne	22-08-17	11:35–11:48	R_C	25.25	1.52	0.03	13.57	0.54	1.52	0.00	MSI
49 Pales	20-08-22	16:33–16:43	R_C	10.95	1.85	0.04	60.35	0.67	-1.84	91.89	MSI
54 Alexandra	23-08-22	10:58–11:05	R_C	15.91	1.26	0.04	77.56	0.98	-1.26	89.44	MSI
54 Alexandra	23-08-24	11:10–11:27	R_C	16.68	1.15	0.06	78.32	1.56	-1.15	89.65	MSI
54 Alexandra	23-09-24	12:31–12:38	R_C	24.69	1.60	0.05	167.10	0.91	1.59	-3.57	MSI
54 Alexandra	23-09-28	10:38–10:52	R_C	25.20	1.23	0.03	162.24	0.76	1.18	-8.18	MSI
58 Concordia	20-03-26	15:15–15:39	R_C	11.64	1.82	0.08	-81.22	1.24	-1.82	-90.91	MSI
58 Concordia	20-05-07	15:30–15:54	R_C	7.49	1.72	0.08	-50.38	1.40	-1.72	90.09	MSI
58 Concordia	20-05-15	15:22–15:41	R_C	10.65	1.90	0.08	-57.18	1.20	-1.90	89.63	MSI
58 Concordia	22-11-28	09:15–12:33	R_C	5.08	1.57	0.03	56.80	0.55	-1.44	101.73	WFGS2
66 Maja	20-03-23	12:17–12:40	R_C	9.43	1.80	0.06	-67.45	1.00	-1.79	87.46	MSI
66 Maja	20-03-26	14:05–16:34	R_C	10.57	1.67	0.24	-59.13	4.04	-1.63	96.43	MSI
66 Maja	20-03-29	16:41–17:20	R_C	11.64	2.02	0.09	-64.23	1.22	-2.02	91.86	MSI
66 Maja	20-04-12	15:16–15:40	R_C	15.70	1.38	0.11	-68.47	2.34	-1.38	89.05	MSI
66 Maja	22-11-06	11:17–12:04	R_C	24.16	0.80	0.08	-19.32	2.97	0.80	0.67	MSI
70 Panopaea	23-08-23	18:07–18:21	R_C	22.76	0.96	0.12	-17.08	3.65	0.93	-6.74	MSI
91 Aegina	23-06-21	13:26–13:48	R_C	8.88	1.52	0.06	-83.88	1.14	-1.52	90.95	MSI
95 Arethusa	22-11-28	10:56–11:41	R_C	19.84	0.48	0.61	-65.12	36.29	0.02	-43.96	WFGS2
95 Arethusa	23-08-23	17:47–18:01	R_C	22.75	0.57	0.06	-15.18	2.91	0.56	-5.54	MSI
99 Dike	20-03-30	17:01–17:25	R_C	8.86	1.63	0.05	-37.01	0.94	-1.34	72.65	MSI
99 Dike	20-04-12	14:08–16:24	R_C	13.55	2.18	0.04	-47.90	0.54	-2.16	85.42	MSI
99 Dike	22-11-28	10:07–10:35	R_C	4.04	0.85	0.14	-70.46	4.84	-0.81	99.38	WFGS2
105 Artemis	22-11-28	15:17–15:17	R_C	11.32	1.47	0.99	23.64	19.33	-1.33	77.53	WFGS2
111 Ate	23-06-21	11:45–12:04	R_C	23.13	0.69	0.08	24.72	3.30	0.69	1.05	MSI
111 Ate	23-06-26	11:05–11:26	R_C	22.70	0.81	0.12	35.42	4.50	0.74	11.33	MSI
128 Nemesis	22-08-07	16:22–16:28	R_C	17.40	0.62	0.13	76.24	6.09	-0.62	-89.12	MSI
142 Polana	23-06-25	16:10–16:35	R_C	23.27	2.24	0.15	-22.18	1.89	2.24	0.83	MSI
144 Vibia	23-06-24	17:00–17:09	R_C	27.00	2.36	0.06	-23.84	0.74	2.36	-1.06	MSI
144 Vibia	23-08-30	18:22–18:44	R_C	28.93	3.44	0.11	-13.31	0.89	3.43	-0.62	MSI
144 Vibia	23-09-01	19:16–19:29	R_C	28.71	3.36	0.16	-13.73	1.33	3.36	-1.34	MSI
147 Protogeneia	20-08-13	16:12–16:22	R_C	10.17	0.91	0.17	61.23	5.35	-0.90	88.84	MSI
147 Protogeneia	20-08-21	15:14–15:25	R_C	7.57	1.14	0.08	59.92	1.98	-1.14	89.56	MSI
147 Protogeneia	20-08-23	15:57–16:21	R_C	6.87	0.86	0.06	67.13	1.85	-0.83	97.55	MSI
162 Laurentia	20-08-02	18:31–18:44	R_C	14.79	1.69	0.38	69.46	6.39	-1.69	89.85	MSI
162 Laurentia	20-08-17	16:18–16:46	R_C	3.35	1.45	0.15	70.85	2.89	-0.88	116.36	MSI
162 Laurentia	20-08-21	17:06–17:29	R_C	11.32	1.41	0.09	70.10	1.76	-1.41	87.93	MSI
162 Laurentia	20-08-23	15:21–15:50	R_C	10.87	1.56	0.08	74.96	1.54	-1.55	92.42	MSI
162 Laurentia	20-08-25	15:37–15:53	R_C	10.38	1.61	0.14	75.05	2.40	-1.61	92.09	MSI
162 Laurentia	20-10-13	12:42–13:06	R_C	5.45	1.21	0.07	55.11	1.67	-1.21	90.36	MSI
173 Ino	23-09-01	18:58–19:02	R_C	26.99	2.47	0.07	-10.52	0.84	2.46	-2.79	MSI
176 Iduna	23-06-25	14:09–14:23	R_C	10.05	1.92	0.07	-40.10	1.07	-1.92	92.20	MSI
176 Iduna	23-07-01	14:20–14:58	R_C	11.19	1.72	0.08	-49.14	1.34	-1.72	89.93	MSI
207 Hedda	23-06-20	14:18–14:37	R_C	9.52	1.62	0.07	86.48	1.24	-1.62	90.04	MSI
207 Hedda	23-06-24	14:15–14:39	R_C	11.41	1.57	0.06	89.52	1.04	-1.57	90.25	MSI
207 Hedda	23-06-26	14:24–14:38	R_C	12.32	1.50	0.08	-88.31	1.50	-1.49	91.32	MSI
209 Dido	23-06-26	14:47–15:01	R_C	8.18	1.12	0.09	-83.88	2.20	-1.11	86.13	MSI
233 Asterope	23-06-19	16:02–16:13	R_C	25.03	0.60	0.06	-27.01	3.06	0.60	-3.65	MSI
238 Hypatia	20-05-12	11:25–11:35	V	17.68	1.09	0.23	-87.51	6.08	-1.01	78.52	MSI
238 Hypatia	23-06-21	15:30–16:26	R_C	21.71	0.07	0.06	1.59	38.15	0.03	25.18	MSI
238 Hypatia	23-09-02	16:35–16:41	R_C	8.14	1.33	0.06	48.11	1.26	-1.26	80.22	MSI
240 Vanadis	23-08-21	10:45–11:09	R_C	7.35	1.40	0.06	71.43	1.16	-1.40	89.89	MSI
257 Silesia	20-08-13	15:49–16:01	R_C	10.39	1.60	0.14	79.34	2.53	-1.56	96.50	MSI
257 Silesia	20-08-21	15:37–15:54	R_C	7.81	1.57	0.08	76.45	1.44	-1.57	90.76	MSI

continued from previous page

Target	Date (YY-MM-DD)	UT	Filter	α^a (deg)	P^b (%)	σP^c (%)	θ^d (deg)	$\sigma\theta^e$ (deg)	P_r^f (%)	θ_r^g (deg)	Inst ^h
257 Silesia	20-08-23	17:26–17:40	R_C	7.10	1.44	0.10	78.60	1.94	-1.44	91.82	MSI
266 Aline	23-06-20	13:01–13:27	R_C	13.00	1.34	0.07	-75.09	1.54	-1.33	87.23	MSI
266 Aline	23-06-21	14:06–14:46	R_C	13.26	1.29	0.11	-74.71	2.36	-1.28	87.56	MSI
266 Aline	23-06-24	12:38–13:02	R_C	13.96	1.29	0.08	-72.31	1.83	-1.28	89.83	MSI
266 Aline	23-06-25	14:30–14:53	R_C	14.20	1.24	0.40	-74.54	9.81	-1.17	87.57	MSI
266 Aline	23-06-26	12:44–14:15	R_C	14.41	1.02	0.07	-72.75	2.06	-1.02	89.32	MSI
266 Aline	23-07-01	12:35–13:28	R_C	15.42	1.25	0.11	-72.06	2.52	-1.25	89.92	MSI
282 Clorinde	23-08-21	14:30–15:42	R_C	8.13	1.03	0.10	77.07	2.67	-1.02	89.27	MSI
284 Amalia	23-06-21	12:49–13:19	R_C	25.49	1.45	0.08	14.20	1.51	1.41	-6.44	MSI
308 Polyxo	20-07-31	16:17–16:26	R_C	10.27	1.57	0.05	62.68	0.89	-1.57	91.63	MSI
308 Polyxo	20-08-08	18:18–18:42	R_C	7.06	1.33	0.09	54.11	1.92	-1.32	86.73	MSI
308 Polyxo	20-08-09	18:30–18:30	R_C	6.65	1.38	0.55	56.48	11.35	-1.38	89.82	MSI
308 Polyxo	20-08-17	16:52–17:06	R_C	3.34	0.73	0.05	46.59	2.09	-0.73	92.16	MSI
308 Polyxo	20-08-21	18:18–18:26	R_C	1.83	0.39	0.09	23.33	6.82	-0.39	92.54	MSI
308 Polyxo	20-10-13	11:56–12:21	R_C	17.85	0.79	0.04	78.38	1.55	-0.77	96.50	MSI
357 Ninina	23-06-20	13:37–14:05	R_C	8.21	1.48	0.06	-39.93	1.13	-1.48	91.04	MSI
357 Ninina	23-07-01	13:36–14:13	R_C	10.65	1.51	0.09	-54.82	1.73	-1.51	90.33	MSI
368 Haidea	23-06-22	16:20–17:30	R_C	24.32	1.93	0.18	-26.89	2.62	1.91	-3.39	MSI
375 Ursula	20-08-02	18:12–18:22	R_C	15.03	0.93	0.06	70.92	1.69	-0.91	96.34	MSI
375 Ursula	20-08-09	18:10–18:22	R_C	13.04	1.07	0.10	64.98	2.61	-1.07	91.80	MSI
375 Ursula	20-08-16	15:17–17:37	R_C	10.80	1.50	0.17	68.00	3.29	-1.45	97.00	MSI
375 Ursula	20-08-21	16:45–16:55	R_C	9.06	1.12	0.04	61.24	1.10	-1.11	92.68	MSI
398 Admete	20-07-30	17:26–17:50	R_C	9.61	1.48	0.14	50.30	2.71	-1.48	90.77	MSI
398 Admete	20-08-21	16:02–17:53	R_C	4.05	0.82	0.09	-25.54	3.26	-0.78	80.36	MSI
398 Admete	20-08-24	14:40–15:04	R_C	4.18	0.91	0.20	-38.02	6.19	-0.89	85.10	MSI
405 Thia	20-07-30	16:31–17:11	R_C	15.11	1.33	0.05	51.32	1.02	-1.33	89.79	MSI
405 Thia	20-08-09	14:44–16:24	R_C	12.59	1.37	0.37	43.75	7.75	-1.37	89.16	MSI
405 Thia	20-08-13	15:32–15:43	R_C	11.49	1.51	0.06	38.96	1.21	-1.50	88.13	MSI
405 Thia	20-08-21	18:00–18:13	R_C	9.23	1.60	0.08	28.80	1.48	-1.60	88.45	MSI
405 Thia	20-08-25	15:59–16:29	R_C	8.18	1.46	0.08	23.15	1.61	-1.46	89.94	MSI
405 Thia	23-06-20	12:29–12:51	R_C	31.23	3.68	0.06	23.24	0.47	3.68	-0.27	MSI
410 Chloris	23-06-21	12:24–12:42	R_C	25.81	1.76	0.08	20.26	1.34	1.75	-3.39	MSI
442 Eichsfeldia	23-11-02	15:14–15:54	R_C	8.46	1.59	0.06	110.72	1.05	-1.54	97.33	MSI
490 Veritas	20-07-31	14:52–15:06	R_C	9.79	1.60	0.16	-73.77	2.91	-1.60	89.09	MSI
490 Veritas	20-08-22	12:36–12:50	R_C	15.09	1.46	0.08	-84.12	1.58	-1.46	90.47	MSI
490 Veritas	22-11-28	13:18–14:17	R_C	12.97	1.10	0.11	-66.50	2.77	-1.09	-86.82	WFGS2
503 Evelyn	20-04-11	14:36–14:59	R_C	22.69	0.44	0.07	17.67	4.65	0.44	-3.60	MSI
503 Evelyn	20-04-13	14:05–14:29	R_C	22.98	0.24	0.10	5.74	11.35	0.21	-15.32	MSI
503 Evelyn	20-05-07	13:36–14:30	R_C	24.76	1.19	0.11	20.39	2.69	1.18	0.54	MSI
503 Evelyn	20-05-15	13:33–14:44	R_C	24.75	1.38	0.16	13.12	3.41	1.34	-6.66	MSI
586 Thekla	20-07-31	16:36–17:04	R_C	14.00	1.26	0.24	71.07	5.45	-1.23	96.16	MSI
586 Thekla	20-08-12	16:00–16:36	R_C	11.04	2.07	0.19	66.21	2.67	-2.06	92.26	MSI
586 Thekla	20-08-17	15:10–16:01	R_C	9.60	1.76	0.14	60.81	2.21	-1.75	87.47	MSI
586 Thekla	20-08-21	16:21–16:34	R_C	8.35	1.53	0.12	65.24	2.24	-1.52	92.57	MSI
586 Thekla	20-08-26	12:34–13:40	R_C	6.75	1.36	0.12	58.89	2.52	-1.36	87.36	MSI
602 Marianna	20-03-24	15:39–16:03	R_C	9.66	1.55	0.11	-73.64	1.98	-1.55	89.01	MSI
602 Marianna	20-03-29	14:02–14:26	R_C	10.84	1.92	0.11	-72.92	1.66	-1.92	89.60	MSI
602 Marianna	20-04-11	15:39–16:03	R_C	13.36	1.55	0.25	-80.69	4.71	-1.48	81.46	MSI
602 Marianna	20-04-13	14:58–15:21	R_C	13.67	1.62	0.26	-62.50	4.56	-1.53	99.58	MSI
602 Marianna	23-06-19	16:22–16:32	R_C	24.57	1.19	0.07	-27.46	1.72	1.18	-4.04	MSI
618 Elfriede	23-06-26	12:29–12:29	R_C	5.29	1.12	0.60	53.10	18.34	-0.80	74.08	MSI
771 Libera	20-08-22	15:58–16:25	R_C	11.31	1.14	0.17	-70.71	4.19	-1.14	88.64	MSI
776 Berbericia	20-03-23	12:56–13:20	R_C	8.03	1.62	0.05	-3.50	0.86	-1.60	85.22	MSI
776 Berbericia	20-03-26	12:58–13:22	R_C	8.41	1.66	0.05	-10.38	0.85	-1.64	85.32	MSI
776 Berbericia	20-03-29	15:28–16:12	R_C	8.89	1.76	0.04	-18.38	0.67	-1.72	83.84	MSI
776 Berbericia	20-04-12	12:28–13:06	R_C	11.45	1.92	0.06	-36.85	0.88	-1.90	86.55	MSI
776 Berbericia	20-05-07	14:51–15:15	R_C	15.55	1.50	0.08	-56.61	1.55	-1.49	86.40	MSI
776 Berbericia	20-05-15	16:02–16:26	R_C	16.41	1.56	0.21	-56.23	3.80	-1.56	90.61	MSI
776 Berbericia	23-09-02	16:49–16:55	R_C	22.82	0.77	0.10	-27.37	3.56	0.52	-23.76	MSI
821 Fanny	23-06-24	13:44–14:07	R_C	11.63	1.34	0.12	56.80	2.56	-1.32	85.86	MSI

continued from previous page

Target	Date (YY-MM-DD)	UT	Filter	α^a (deg)	P^b (%)	σP^c (%)	θ^d (deg)	$\sigma\theta^e$ (deg)	P_r^f (%)	θ_r^g (deg)	Inst ^h
821 Fanny	23-06-26	15:21–15:50	R_C	10.75	1.18	0.11	60.36	2.71	-1.17	91.33	MSI
1015 Christa	23-06-25	12:39–13:02	R_C	10.76	1.19	0.10	-57.28	2.53	-1.15	96.76	MSI
1201 Strenua	23-06-25	13:11–14:03	R_C	11.72	0.93	0.18	-69.09	5.65	-0.91	87.20	MSI
1542 Schalen	23-09-24	12:45–13:09	R_C	9.68	1.16	0.08	78.87	2.04	-1.07	101.73	MSI
1754 Cunningham	23-06-19	15:25–15:40	R_C	7.48	0.80	0.12	-40.78	4.44	-0.79	89.64	MSI
1754 Cunningham	23-06-24	13:10–13:33	R_C	8.60	1.14	0.10	-46.02	2.50	-1.14	92.15	MSI
1795 Woltjer	20-08-22	15:22–15:27	R_C	10.57	2.17	0.26	-73.34	3.43	-2.09	97.47	MSI
1867 Deiphobus	23-09-24	16:21–17:12	R_C	6.82	0.48	0.11	116.18	6.84	-0.47	91.23	MSI
2569 Madeline	23-09-24	14:27–14:46	R_C	8.85	1.29	0.07	145.12	1.47	-1.29	88.78	MSI

Notes. ^(a) Median solar phase angle in degrees, ^(b) Nightly weighted averaged polarization degree in percent, ^(c) Weighted mean error of P in percent, ^(d) Position angle of the strongest electric vector in degree, ^(e) Error of θ in degree, ^(f) Polarization degree referring to the scattering plane in percent, ^(g) Position angle referring to the scattering plane in degree, ^(h) Instrument

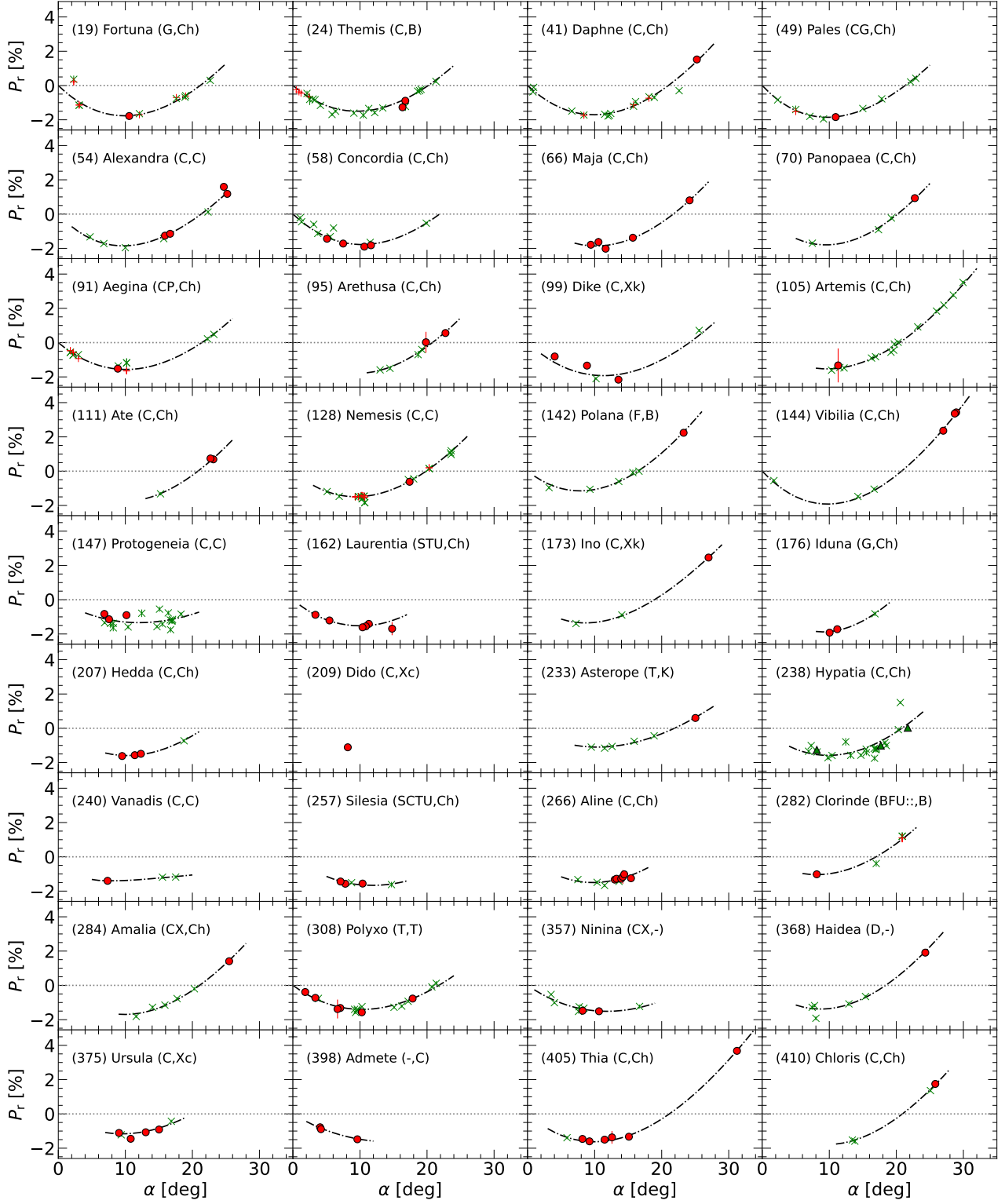


Fig. D3. Phase angle dependence of linear polarization degree (P_r) of the 52 asteroids observed in this study. Red-filled circle and green-filled triangle markers are $P_r(\alpha)$ obtained in this study in R_C - and V -bands, respectively. $P_r(\alpha)$ data from Cellino et al. (2015), Devogèle et al. (2017), Gil-Hutton, R. & García-Migani, E. (2017), Lupishko (2018), López-Sisterna et al. (2019), and Bendjoya et al. (2022) taken in V (green cross markers)- or R_C (red plus markers)-bands are shown. We show the polarization phase curves fitted using data from this study and literature by exponential functions with the dashed-dotted line.

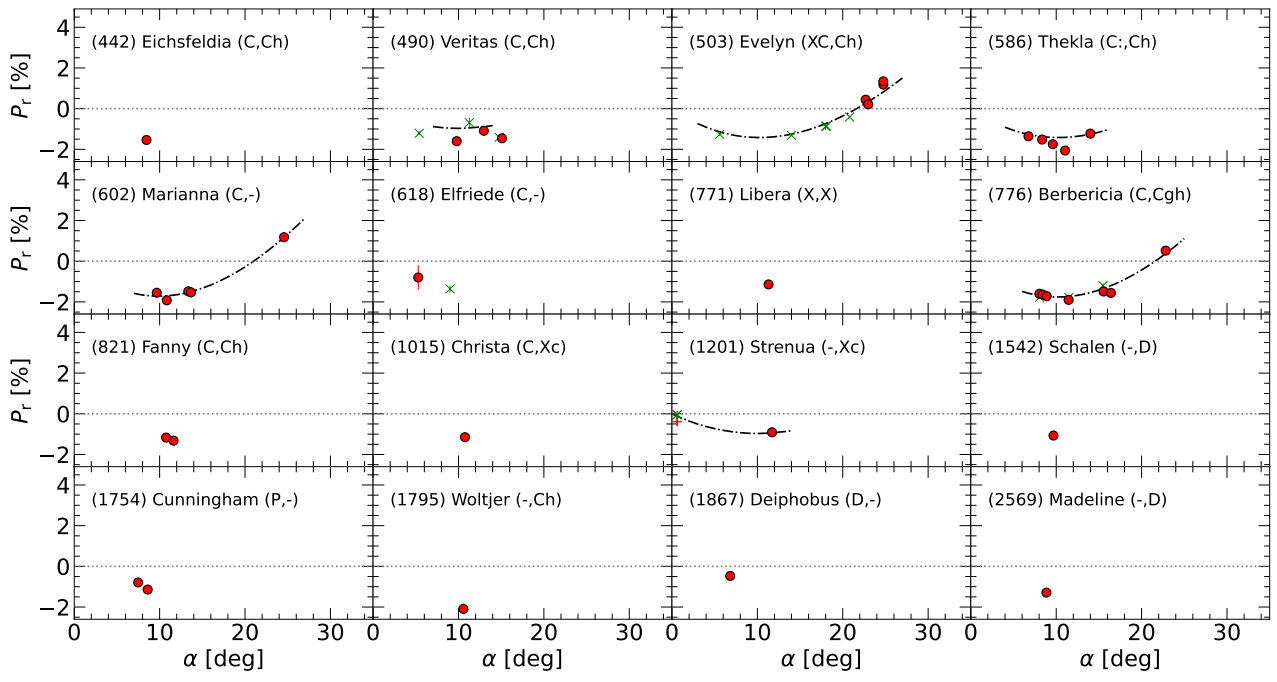


Fig. D4. Continued figures of Fig. D3